arXiv:1405.5245v1 [math.NA] 20 May 2014

An accurate and efficient numerical framework for adaptive numerical weather prediction

Giovanni Tumolo[(1)], Luca Bonaventura[(2)]

May 22, 2014

[(1)] Earth System Physics Section
The Abdus Salam International Center for Theoretical Physics
Strada Costiera 11, 34151 Trieste, Italy
gtumolo@ictp.it

[(2)] MOX – Modelling and Scientific Computing,
Dipartimento di Matematica "F. Brioschi", Politecnico di Milano
Via Bonardi 9, 20133 Milano, Italy
luca.bonaventura@polimi.it

Keywords: Discontinuous Galerkin methods, adaptive finite elements, semi-implicit discretizations, semi-Lagrangian discretizations, shallow water equations, Euler equations.

AMS Subject Classification: 35L02, 65M60, 65M25, 76U05, 86A10

Abstract

We present an accurate and efficient discretization approach for the adaptive discretization of typical model equations employed in numerical weather prediction. A semi-Lagrangian approach is combined with the TR-BDF2 semi-implicit time discretization method and with a spatial discretization based on adaptive discontinuous finite elements. The resulting method has full second order accuracy in time and can employ polynomial bases of arbitrarily high degree in space, is unconditionally stable and can effectively adapt the number of degrees of freedom employed in each element, in order to balance accuracy and computational cost. The $p-$adaptivity approach employed does not require remeshing, therefore it is especially suitable for applications, such as numerical weather prediction, in which a large number of physical quantities are associated with a given mesh. Furthermore, although the proposed method can be implemented on arbitrary unstructured and nonconforming meshes, even its application on simple Cartesian meshes in spherical coordinates can cure effectively the pole problem by reducing the polynomial degree used in the polar elements. Numerical simulations of classical benchmarks for the shallow water and for the fully compressible Euler equations validate the method and demonstrate its capability to achieve accurate results also at large Courant numbers, with time steps up to 100 times larger than those of typical explicit discretizations of the same problems, while reducing the computational cost thanks to the adaptivity algorithm.

1 Introduction

The Discontinuous Galerkin (DG) spatial discretization approach is currently being employed by an increasing number of environmental fluid dynamics models see e.g. [12], [17], [28],[39],[19],[25] and a more complete overview in [5]. This is motivated by the many attractive features of DG discretizations, such as high order accuracy, local mass conservation and ease of massively parallel implementation.

On the other hand, DG methods imply severe stability restrictions when coupled with explicit time discretizations. One traditional approach to overcome stability restrictions in low Mach number problems is the combination of semi - implicit (SI) and semi - Lagrangian (SL) techniques. In a series of papers [41], [42], [19], [14], [52] it has been shown that most of the computational gains traditionally achieved in finite difference models by the application of SI, SL and SISL discretization methods are also attainable in the framework of DG approaches. In particular, in [52] we have introduced a dynamically $p-$adaptive SISL-DG discretization approach for low Mach number problems, that is quite effective in achieving high order spatial accuracy, while reducing substantially the computational cost.

In this paper, we apply the technique of [52] to the shallow water equations in spherical geometry and to the the fully compressible Euler equations, in order to show its effectiveness for model problems typical of global and regional weather forecasting. The advective form of the equations of motion is employed and the semi-implicit time discretization is based on the TR-BDF2 method, see e.g. [21], [32]. This combination of two robust ODE solvers yields a second order accurate, A-stable and L-stable method (see e.g. [27]), that is effective in damping selectively high frequency modes. At the same time, it achieves full second order accuracy, while the off-centering in the trapezoidal rule, typically necessary for realistic applications to nonlinear problems (see e.g. [7], [11], [52]), limits the accuracy in time to first order. Numerical results presented in this paper show that the total computational cost of one TR-BDF2 step is analogous to that of one step of the off-centered trapezoidal rule, as well as the structure of the linear problems to be solved at each time step, thus allowing to extend naturally to this more accurate method any implementation based on the off-centered trapezoidal rule. Numerical simulations of the shallow water benchmarks proposed in [55], [29], [22] and of the non-hydrostatic benchmarks proposed in [47], [23] have been employed to validate the method and to demonstrate its capabilities. In particular, it will be shown that the present approach enables the use of time steps even 100 times larger than those allowed for DG models by

standard explicit schemes, see e.g. the results in [38].

The method presented in this paper, just as its previous version in [52], can be applied in principle on arbitrarily unstructured and even nonconforming meshes. For example, a model based on this method could run on a non conforming mesh of rectangular elements built around the nodes of a reduced Gaussian grid [20]. For simplicity, however, no such implementation has been developed so far. Here, only a simple Cartesian mesh has been used. If no degree adaptivity is employed, this results in very high Courant numbers in the polar regions. These do not result in any special stability problems for the present SISL discretization approach, as it will be shown by the numerical results reported below. On the other hand, even with an implementation based on a simple Cartesian mesh in spherical coordinates, the flexibility of the DG space discretization allows to reduce the degree of the basis and test functions employed close to the poles, thus making the effective model resolution more uniform and solving the efficiency issues related to the pole problem by static $p-$adaptivity. This is especially advantageous because the conditioning of the linear system to be solved at each time step is greatly improved and, as a consequence, the number of iterations necessary for the linear solver is reduced by approximately 80%, while at the same time no spurious reflections nor artificial error increases are observed.

Beyond these computational advantages, we believe that the present approach based on $p-$adaptivity is especially suitable for applications to numerical weather prediction, in contrast to $h-$adaptivity approaches (that is, local mesh coarsening or refinement in which the size of some elements changes in time). Indeed, in numerical weather prediction, information that is necessary to carry out realistic simulations (such as orography profiles, data on land use and soil type, land-sea masks) needs to be reconstructed on the computational mesh and has to be re-interpolated each time that the mesh is changed. Furthermore, many physical parameterizations are highly sensitive to the mesh size. Although devising better parameterizations that require less mesh-dependent tuning is an important research goal, more conventional parameterizations will still be in use for quite some time. As a consequence, it is useful to improve the accuracy locally by adding supplementary degrees of freedom where necessary, as done in a $p-$adaptive framework, without having to change the underlying computational mesh. In conclusion, the resulting modeling framework seems to be able to combine the efficiency and high order accuracy of traditional SISL pseudo-spectral methods with the locality and flexibility of more standard DG approaches.

In section 2, two examples of governing equations are introduced.

In section 3, the TR-BDF2 method is reviewed. In section 4 the approach employed for the advection of vector fields in spherical geometry is described in detail. In section 5, we introduce the SISL-DG discretization approach for the shallow water equations in spherical geometry. In section 6, we outline its extension to the fully compressible Euler equations in a vertical plane. Numerical results are presented in section 7, while in section 8 we try to draw some conclusions and outline the path towards application of the concepts introduced here in the context of a non hydrostatic dynamical core.

2 Governing equations

We consider as a basic model problem the two-dimensional shallow water equations on a rotating sphere (see e.g. [15]). These equations are a standard test bed for numerical methods to be applied to the full equations of motion of atmospheric or oceanic circulation models, see e.g. [55]. Among their possible solutions, they admit Rossby and inertial gravity waves, as well as the response of such waves to orographic forcing. We will use the advective, vector form of the shallow water equations:

$$\frac{Dh}{Dt} = -h\nabla \cdot \mathbf{u}, \tag{1}$$

$$\frac{D\mathbf{u}}{Dt} = -g\nabla h - f\hat{\mathbf{k}} \times \mathbf{u} - g\nabla b. \tag{2}$$

Here h represents the fluid depth, b the bathymetry elevation, f the Coriolis parameter, $\hat{\mathbf{k}}$ the unit vector locally normal to the Earth's surface and g the gravity force per unit mass on the Earth's surface. Assuming that x, y are orthogonal curvilinear coordinates on the sphere (or on a portion of it), we denote by m_x and m_y the components of the (diagonal) metric tensor. Furthermore, we set $\mathbf{u} = (u, v)^T$, where u and v are the contravariant components of the velocity vector in the coordinate direction x and y respectively, multiplied by the corresponding metric tensor components. We also denote by $\frac{D}{Dt}$ the Lagrangian derivative

$$\frac{D}{Dt} = \frac{\partial}{\partial t} + \frac{u}{m_x}\frac{\partial}{\partial x} + \frac{v}{m_y}\frac{\partial}{\partial y},$$

so that $u = m_x\frac{Dx}{Dt}, v = m_y\frac{Dy}{Dt}$. In particular, in this paper standard spherical coordinates will be employed.

As an example of a more complete model, we will also consider the fully compressible, non hydrostatic equations of motion. Following

e.g. [10], [4], [11], they can be written as

$$\begin{aligned}
\frac{D\Pi}{Dt} &= -\left(\frac{c_p}{c_v} - 1\right)\Pi\nabla\cdot\mathbf{u},\\
\frac{D\mathbf{u}}{Dt} &= -c_p\Theta\nabla\Pi - g\hat{\mathbf{k}},\\
\frac{D\Theta}{Dt} &= 0.
\end{aligned}$$

where, being p_0 a reference pressure value, $\Theta = T\left(\frac{p}{p_0}\right)^{-R/c_p}$ is the potential temperature, $\Pi = \left(\frac{p}{p_0}\right)^{R/c_p}$ is the Exner pressure, while c_p, c_v, R are the constant pressure and constant volume specific heats and the gas constant of dry air respectively. Here the Coriolis force is omitted for simplicity. Notice also that, by a slight abuse of notation, in the three-dimensional case $\mathbf{u} = (u, v, w)^T$ denotes the three dimensional velocity field and the $\frac{D}{Dt}$, ∇ operators are also three-dimensional, while we will assume $\mathbf{u} = (u, w)^T$ in the description of (x, z) two dimensional, vertical slice models. It is customary to rewrite such equations in terms of perturbations with respect to a steady hydrostatic reference profile, so that assuming $\Pi(x, y, z, t) = \pi^*(z) + \pi(x, y, z, t)$, $\Theta(x, y, z, t) = \theta^*(z) + \theta(x, y, z, t)$ with $c_p\theta^*\frac{d\pi^*}{dz} = -g$, one obtains for a vertical plane

$$\frac{D\Pi}{Dt} = -\left(\frac{c_p}{c_v} - 1\right)\Pi\nabla\cdot\mathbf{u}, \tag{3}$$

$$\frac{Du}{Dt} = -c_p\Theta\frac{\partial\pi}{\partial x}, \tag{4}$$

$$\frac{Dw}{Dt} = -c_p\Theta\frac{\partial\pi}{\partial z} + g\frac{\theta}{\theta^*}, \tag{5}$$

$$\frac{D\theta}{Dt} = -\frac{d\theta^*}{dz}w. \tag{6}$$

It can be observed that equations (3)-(6) are isomorphic to equations (1)-(2), which will allow to extend almost automatically the discretization approach proposed for the former to the more general model.

3 Review of the TR-BDF2 method

We review here some properties of the so called TR-BDF2 method, which was first introduced in [2]. Given a Cauchy problem

$$\begin{aligned}
\mathbf{y}' &= \mathbf{f}(\mathbf{y}, t)\\
\mathbf{y}(0) &= \mathbf{y}_0
\end{aligned} \tag{7}$$

and considering a time discretization employing a constant time step Δt, the TR-BDF2 method is defined by the two following implicit stages:

$$\begin{aligned} \mathbf{u}^{n+2\gamma} - \gamma\Delta t\mathbf{f}(\mathbf{u}^{n+2\gamma}, t_n + 2\gamma\Delta t) &= \mathbf{u}^n + \gamma\Delta t\mathbf{f}(\mathbf{u}^n, t_n), \\ \mathbf{u}^{n+1} - \gamma_2\Delta t\mathbf{f}(\mathbf{u}^{n+1}, t_{n+1}) &= (1-\gamma_3)\mathbf{u}^n + \gamma_3\mathbf{u}^{n+2\gamma}. \end{aligned} \quad (8)$$

Here $\gamma \in [0, 1/2]$ is an implicitness parameter and

$$\gamma_2 = \frac{1-2\gamma}{2(1-\gamma)}, \quad \gamma_3 = \frac{1-\gamma_2}{2\gamma}.$$

It is immediate that the first stage of (8) is simply the application of the trapezoidal rule (or Crank-Nicolson method) over the interval $[t_n, t_n + 2\gamma\Delta t]$. It could also be substituted by an off centered Crank-Nicolson step without reducing the overall accuracy of the method. The outcome of this stage is then used to turn the two step BDF2 method into a single step, two stages method. This combination of two robust stiff solvers yields a method with several interesting accuracy and stability properties, that were analyzed in detail in [21]. As shown in this paper, this analysis is most easily carried out by rewriting the method as

$$\begin{aligned} \mathbf{k}_1 &= \mathbf{f}\left(\mathbf{u}^n, t_n\right) \\ \mathbf{k}_2 &= \mathbf{f}\left(\mathbf{u}^n + \gamma\Delta t\mathbf{k}_1 + \gamma\Delta t\mathbf{k}_2, t_n + \gamma\Delta t\right) \\ \mathbf{k}_3 &= \mathbf{f}\left(\mathbf{u}^n + \frac{1-\gamma}{2}\Delta t\mathbf{k}_1 + \frac{1-\gamma}{2}\Delta t\mathbf{k}_2 + \gamma\Delta t\mathbf{k}_3, t_{n+1}\right) \\ \mathbf{u}^{n+1} &= \mathbf{u}^n + \Delta t\left(\frac{1-\gamma}{2}\mathbf{k}_1 + \frac{1-\gamma}{2}\mathbf{k}_2 + \gamma\mathbf{k}_3\right). \end{aligned} \quad (9)$$

In this formulation, the TR-BDF2 method is clearly a Singly Diagonal Implicit Runge Kutta (SDIRK) method, so that one can rely on the theory for this class of methods to derive stability and accuracy results (see e.g. [27]). Notice that the same method has been rediscovered in [6] and has been analyzed and applied also in [18], to treat the implicit terms in the framework of an Additive Runge Kutta approach (see e.g. [26]). As shown in [21], the TR-BDF2 method is second order accurate and A-stable for any value of γ. Written as in (9), the method can also be proven to constitute a (2,3) embedded Runge-Kutta pair, with companion coefficients given by

$$(1 - \frac{\sqrt{2}}{4})/3, \quad (1 + 3\frac{\sqrt{2}}{4})/3, \quad \frac{2-\sqrt{2}}{6},$$

provided that no off centering is employed in the first stage of (8). This equips the method with an extremely efficient estimator of the time discretization error. Furthermore, for $\gamma = 1 - \sqrt{2}/2$ it is also L-stable. Therefore, with this coefficient value it can be safely applied to problems with eigenvalues whose imaginary part is large, such as typically arise from the discretization of hyperbolic problems. This is not the case for the standard trapezoidal rule (or Crank-Nicolson) implicit method, whose linear stability region is exactly bounded by the imaginary axis. As a consequence, it is common to apply the trapezoidal rule with off centering, see e.g. [7], [11] as well as [52], which results in a first order time discretization. TR-BDF2 appears therefore to be an interesting one step alternative to maintain full second order accuracy, especially considering that, if formulated as (8), it is equivalent to performing two Crank-Nicolson steps with slightly modified coefficients. In order to highlight the advantages of the proposed method in terms of accuracy with respect to other common robust stiff solvers, we plot in figure 1 the contour levels of the absolute value of the linear stability function of the TR-BDF2 method without off centering in the first stage, compared to the analogous contours of the off centered Crank-Nicolson method with averaging parameter $\theta = 0.6, \theta = 0.7$ in figures 2, 3, respectively, and to those of the BDF2 method in figure 4. It is immediate to see that TR-BDF2 introduces less damping around the imaginary axis for moderate values of the time step. On the other hand, TR-BDF2 is more selective in damping very large eigenvalues, as clearly displayed in figure 5, where the absolute values of the linear stability functions of the same methods (with the exception of BDF2, for which an explicit representation of the stability function is not available) are plotted along the imaginary axis.

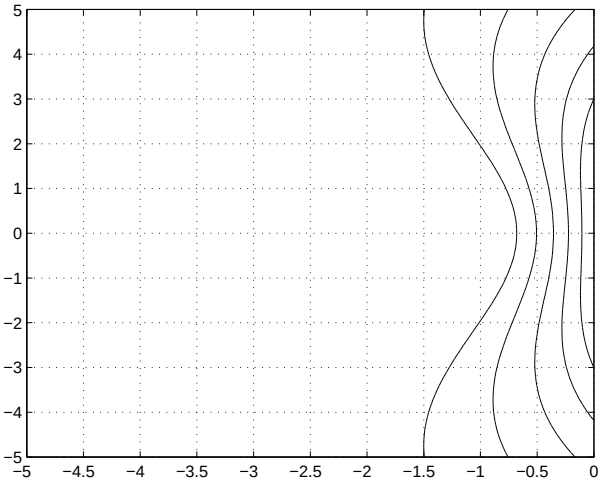

Figure 1: Contour levels of the absolute value of the stability function of the TR-BDF2 method without off centering in the first stage. Contour spacing is 0.1 from 0.5 to 1.

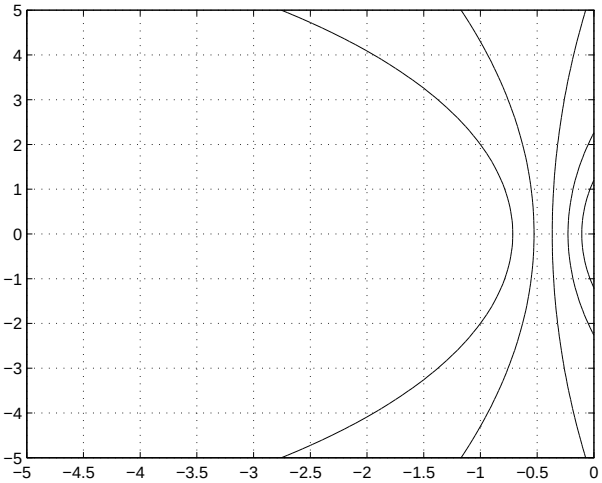

Figure 2: Contour levels of the absolute value of the stability function of the off centered Crank-Nicolson method with averaging parameter $\theta = 0.6$ (equivalent to an off centering parameter valued 0.05). Contour spacing is 0.1 from 0.5 to 1.

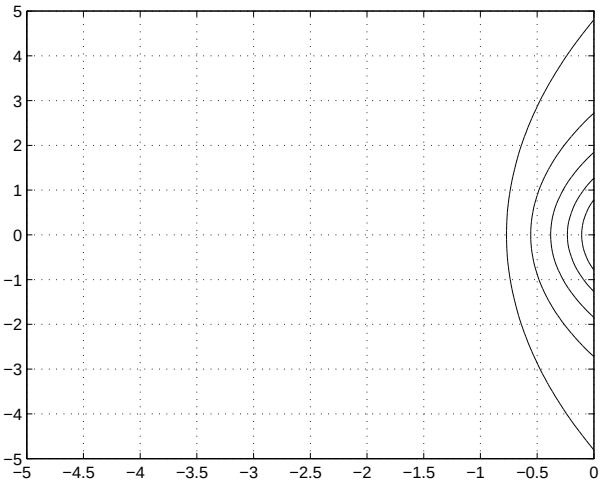

Figure 3: Contour levels of the absolute value of the stability function of the off centered Crank-Nicolson method with averaging parameter $\theta = 0.7$ (equivalent to an off centering parameter valued 0.1). Contour spacing is 0.1 from 0.5 to 1.

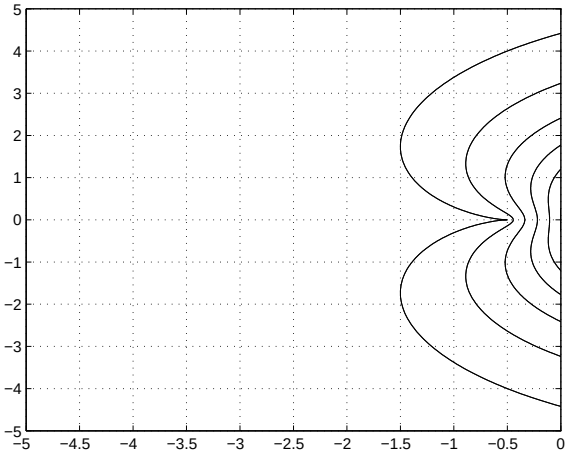

Figure 4: Contour levels of the absolute value of the stability function of the BDF2 method. Contour spacing is 0.1 from 0.5 to 1.

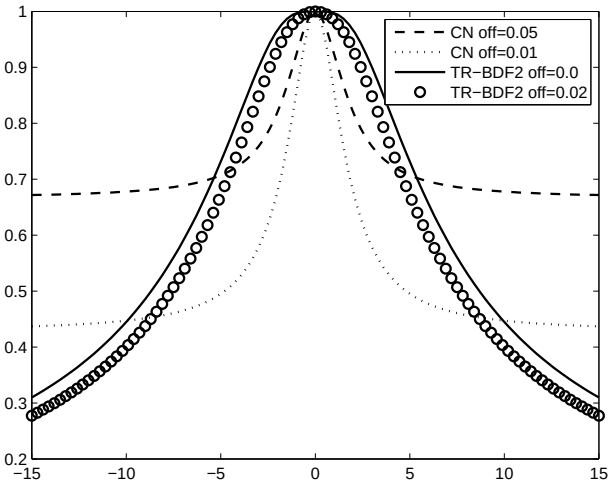

Figure 5: Graph of the absolute value of the stability functions of several L-stable methods along the imaginary axis.

4 Review of Semi-Lagrangian evolution operators for vector fields on the sphere

The semi-Lagrangian method can be described introducing the concept of evolution operator, along the lines of [37, 35]. Indeed, let $G = G(\mathbf{x}, t)$ denote a generic function of space and time that is the solution of

$$\frac{DG}{Dt} = \frac{\partial G}{\partial t} + \frac{u}{m_x}\frac{\partial G}{\partial x} + \frac{v}{m_y}\frac{\partial G}{\partial y} = 0.$$

To approximate this solution on the time interval $[t^n, t^{n+1}]$, a numerical evolution operator E is introduced, that approximates the exact evolution operator associated to the frozen velocity field $\mathbf{u}^* = (u^*, v^*)^T$, that may coincide with the velocity field at time level t^n or with an extrapolation derived from more previous time levels. More precisely, if $\mathbf{X}(t; t^{n+1}, \mathbf{x})$ denotes the solution of

$$\frac{d\mathbf{X}(t; t^{n+1}, \mathbf{x})}{dt} = \mathbf{u}^*(\mathbf{X}(t; t^{n+1}, \mathbf{x})) \tag{10}$$

with initial datum $\mathbf{X}(t^{n+1}; t^{n+1}, \mathbf{x}) = \mathbf{x}$ at time $t = t^{n+1}$, then the expression $[E(t^n, \Delta t)G](\mathbf{x})$ denotes a numerical approximation of $G^n(\mathbf{x}_D)$ where $\mathbf{x}_D = \mathbf{X}(t^n; t^{n+1}, \mathbf{x})$ and the notation $G^n(\mathbf{x}) = G(\mathbf{x}, t^n)$ is used. Since $\mathbf{x}_D$ is nothing but the position at time t^n of the fluid parcel reaching location $\mathbf{x}$ at time t^{n+1}, according to standard terminology, it is called the departure point associated with the arrival point $\mathbf{x}$. Different methods can be employed to approximate $\mathbf{x}_D$; in this paper, for simplicity, the method proposed in [34] has been employed in spherical geometry. Furthermore, to guarantee an accuracy compatible with that of the semi-implicit time-discretization, an extrapolation $\mathbf{u}^{n+\frac{1}{2}}$ of the velocity field at the intermediate time level $t^n + \Delta t/2$ was used as $\mathbf{u}^*$ in (10). On the other hand, in the application to Cartesian geometry (for the vertical slice discretization), a simple first order Euler method with sub-stepping was employed, see e.g. [16], [45].

In case of the advection of a vector field

$$\frac{D\mathbf{G}}{Dt} = \frac{\partial \mathbf{G}}{\partial t} + \frac{u}{m_x}\frac{\partial \mathbf{G}}{\partial x} + \frac{v}{m_y}\frac{\partial \mathbf{G}}{\partial y} = 0,$$

as in the momentum equation (2), the extension of this approach has to take into account the curvature of the spherical manifold. More specifically, unit basis vectors at the departure point are not in general aligned with those at the arrival point, i.e., if $\hat{\boldsymbol{i}}, \hat{\boldsymbol{j}}, \hat{\boldsymbol{k}}$ represent a unit vector triad, in general $\hat{\mathbf{i}}(\mathbf{x}) \neq \hat{\boldsymbol{i}}(\mathbf{x}_D)$, $\hat{\boldsymbol{j}}(\mathbf{x}) \neq \hat{\boldsymbol{j}}(\mathbf{x}_D)$, $\hat{\boldsymbol{k}}(\mathbf{x}) \neq \hat{\boldsymbol{k}}(\mathbf{x}_D)$.

To deal with this issue two approaches are available. The first, intrinsically Eulerian, consists in the introduction of the Christoffel symbols in the covariant derivatives definition, giving rise to the well known metric terms, before the SISL discretization, and then in the approximation along the trajectories of those metric terms. This approach has been shown to be source of instabilities in a semi-Lagrangian frame, see e.g. [44, 8, 9, 13] and therefore is not adopted in this work. The second approach, more suitable for semi-Lagrangian discretizations, takes into account the curvature of the manifold only at discrete level, i.e. after the SISL discretization has been performed. Many variations of this idea have been proposed, see e.g. [44, 8, 9, 3, 49]. In [48], they have all been derived in a unified way by the introduction of a proper rotation matrix that transforms vector components in the departure-point unit vector triad $\hat{\boldsymbol{\imath}}_D = \hat{\boldsymbol{\imath}}(\mathbf{x}_D)$, $\hat{\boldsymbol{\jmath}}_D = \hat{\boldsymbol{\jmath}}(\mathbf{x}_D)$, $\hat{\boldsymbol{k}}_D = \hat{\boldsymbol{k}}(\mathbf{x}_D)$ into vector components in the arrival-point unit vector triad $\hat{\boldsymbol{\imath}} = \hat{\boldsymbol{\imath}}(\mathbf{x})$, $\hat{\boldsymbol{\jmath}} = \hat{\boldsymbol{\jmath}}(\mathbf{x})$, $\hat{\boldsymbol{k}} = \hat{\boldsymbol{k}}(\mathbf{x})$. To see how this rotation matrix comes into play, it is sufficient to consider the action of the evolution operator E on a given vector valued function of space and time $\boldsymbol{G}$, defined as an approximation of

$$\left[E(t^n, \Delta t)\boldsymbol{G}\right](\mathbf{x}) = \boldsymbol{G}^n(\mathbf{x}_D), \tag{11}$$

and to write this equation componentwise. $\boldsymbol{G}^n(\mathbf{x}_D)$ is known through its components in the departure point unit vector triad:

$$\boldsymbol{G}^n(\mathbf{x}_D) = \mathcal{G}_x^n(\mathbf{x}_D)\hat{\boldsymbol{\imath}}_D + \mathcal{G}_y^n(\mathbf{x}_D)\hat{\boldsymbol{\jmath}}_D + \mathcal{G}_z^n(\mathbf{x}_D)\hat{\boldsymbol{k}}_D. \tag{12}$$

Therefore, via (11), the components of $\left[E(t^n, \Delta t)\boldsymbol{G}\right](\mathbf{x})$ in the unit vector triad at the same point are given by projection of (12) along $\hat{\boldsymbol{\imath}}$, $\hat{\boldsymbol{\jmath}}$, $\hat{\boldsymbol{k}}$:

$$\begin{aligned}
\hat{\boldsymbol{\imath}} \cdot \boldsymbol{G}^n(\mathbf{x}_D) &= \mathcal{G}_x^n(\mathbf{x}_D)\, \hat{\boldsymbol{\imath}} \cdot \hat{\boldsymbol{\imath}}_D + \mathcal{G}_y^n(\mathbf{x}_D)\, \hat{\boldsymbol{\imath}} \cdot \hat{\boldsymbol{\jmath}}_D + \mathcal{G}_z^n(\mathbf{x}_D)\, \hat{\boldsymbol{\imath}} \cdot \hat{\boldsymbol{k}}_D, \\
\hat{\boldsymbol{\jmath}} \cdot \boldsymbol{G}^n(\mathbf{x}_D) &= \mathcal{G}_x^n(\mathbf{x}_D)\, \hat{\boldsymbol{\jmath}} \cdot \hat{\boldsymbol{\imath}}_D + \mathcal{G}_y^n(\mathbf{x}_D)\, \hat{\boldsymbol{\jmath}} \cdot \hat{\boldsymbol{\jmath}}_D + \mathcal{G}_z^n(\mathbf{x}_D)\, \hat{\boldsymbol{\jmath}} \cdot \hat{\boldsymbol{k}}_D, \\
\hat{\boldsymbol{k}} \cdot \boldsymbol{G}^n(\mathbf{x}_D) &= \mathcal{G}_x^n(\mathbf{x}_D)\hat{\boldsymbol{k}} \cdot \hat{\boldsymbol{\imath}}_D + \mathcal{G}_y^n(\mathbf{x}_D)\hat{\boldsymbol{k}} \cdot \hat{\boldsymbol{\jmath}}_D + \mathcal{G}_z^n(\mathbf{x}_D)\hat{\boldsymbol{k}} \cdot \hat{\boldsymbol{k}}_D,
\end{aligned}$$

i.e., in matrix notation:

$$\begin{pmatrix}
\hat{\boldsymbol{\imath}} \cdot \left[E(t^n, \Delta t)\boldsymbol{G}\right](\mathbf{x}) \\
\hat{\boldsymbol{\jmath}} \cdot \left[E(t^n, \Delta t)\boldsymbol{G}\right](\mathbf{x}) \\
\hat{\boldsymbol{k}} \cdot \left[E(t^n, \Delta t)\boldsymbol{G}\right](\mathbf{x})
\end{pmatrix} = \mathbf{R} \begin{pmatrix}
\mathcal{G}_x^n \\ \mathcal{G}_y^n \\ \mathcal{G}_z^n
\end{pmatrix} \qquad \text{where}$$

$$\mathbf{R} = \begin{bmatrix}
\hat{\boldsymbol{\imath}} \cdot \hat{\boldsymbol{\imath}}_D & \hat{\boldsymbol{\imath}} \cdot \hat{\boldsymbol{\jmath}}_D & \hat{\boldsymbol{\imath}} \cdot \hat{\boldsymbol{k}}_D \\
\hat{\boldsymbol{\jmath}} \cdot \hat{\boldsymbol{\imath}}_D & \hat{\boldsymbol{\jmath}} \cdot \hat{\boldsymbol{\jmath}}_D & \hat{\boldsymbol{\jmath}} \cdot \hat{\boldsymbol{k}}_D \\
\hat{\boldsymbol{k}} \cdot \hat{\boldsymbol{\imath}}_D & \hat{\boldsymbol{k}} \cdot \hat{\boldsymbol{\jmath}}_D & \hat{\boldsymbol{k}} \cdot \hat{\boldsymbol{k}}_D
\end{bmatrix}.$$

Under the shallow atmosphere approximation [51], $\mathbf{R}$ can be reduced to the 2×2 rotation matrix

$$\mathbf{\Lambda} = \mathbf{\Lambda}(\mathbf{x}, \mathbf{x}_D) = \begin{bmatrix} \Lambda_{11} & \Lambda_{12} \\ \Lambda_{21} & \Lambda_{22} \end{bmatrix}, \tag{13}$$

where, as shown in [48], $\Lambda_{11} = \Lambda_{22} = (R_{11} + R_{22})/(1 + R_{33})$, $\Lambda_{12} = -\Lambda_{21} = (R_{12} - R_{21})/(1 + R_{33})$. Therefore, in the following the evolution operator for vector fields will be defined componentwise as

$$\begin{pmatrix} \hat{\boldsymbol{i}} \cdot [E(t^n, \Delta t)\boldsymbol{G}](\mathbf{x}) \\ \hat{\boldsymbol{j}} \cdot [E(t^n, \Delta t)\boldsymbol{G}](\mathbf{x}) \end{pmatrix} = \mathbf{\Lambda} \begin{pmatrix} \mathcal{G}_x^n(\mathbf{x}_D) \\ \mathcal{G}_y^n(\mathbf{x}_D) \end{pmatrix}. \tag{14}$$

5 A novel SISL time integration approach for the shallow water equations on the sphere

The SISL discretization of equations.(1)-(2) based on (8) is then obtained by performing the two stages in (8) after reinterpretation of the intermediate values in a semi-Lagrangian fashion. Furthermore, in order to avoid the solution of a nonlinear system, the dependency on h in $h\nabla \cdot \mathbf{u}$ is linearized in time, as common in semi-implicit discretizations based on the trapezoidal rule, see e.g. [7],[52]. Numerical experiments reported in the following show that this does not prevent to achieve second order accuracy in the regimes of interest for numerical weather prediction. The TR stage of the SISL time semi-discretization of the equations in vector form (1)-(2) is given by

$$\begin{aligned} h^{n+2\gamma} &+ \gamma \Delta t\, h^n\, \nabla \cdot \mathbf{u}^{n+2\gamma} \\ &= E\left(t^n, 2\gamma\Delta t\right)\left[h - \gamma \Delta t\, h\, \nabla \cdot \mathbf{u}\right], \end{aligned} \tag{15}$$

$$\begin{aligned} &\mathbf{u}^{n+2\gamma} + \gamma\Delta t\Big[g\nabla h^{n+2\gamma} + f\hat{\mathbf{k}} \times \mathbf{u}^{n+2\gamma}\Big] = -\gamma\Delta t\, g\nabla b \\ &+E\big(t^n, 2\gamma\Delta t\big)\left\{\mathbf{u} - \gamma\Delta t\left[g(\nabla h + \nabla b) + f\hat{\mathbf{k}} \times \mathbf{u}\right]\right\}. \end{aligned} \tag{16}$$

The TR stage is then followed by the BDF2 stage:

$$\begin{aligned} h^{n+1} &+ \gamma_2 \Delta t\, h^{n+2\gamma}\, \nabla \cdot \mathbf{u}^{n+1} \\ &= \big(1 - \gamma_3\big) E\big(t^n, \Delta t\big) h \\ &+ \gamma_3 E\big(t^n + 2\gamma\Delta t, (1 - 2\gamma)\Delta t\big) h, \end{aligned} \tag{17}$$

$$\mathbf{u}^{n+1} + \gamma_2 \Delta t \Big[g \nabla h^{n+1} + f \hat{\mathbf{k}} \times \mathbf{u}^{n+1} \Big] = -\gamma_2 \Delta t \; g \nabla b$$
$$+ \big(1 - \gamma_3\big) E\big(t^n, \Delta t\big)\mathbf{u} + \gamma_3 E\big(t^n + 2\gamma\Delta t, (1-2\gamma)\Delta t\big)\mathbf{u}. \quad (18)$$

For each of the two stages, the spatial discretization can be performed along the lines described in [52], allowing for variable polynomial order to locally represent the solution in each element. The spatial discretization approach considered is independent of the nature of the mesh and could also be implemented for fully unstructured and even non conforming meshes. For simplicity, however, in this paper only an implementation on a structured mesh in longitude-latitude coordinates has been developed. In principle, either Lagrangian or hierarchical Legendre bases could be employed. We will work almost exclusively with hierarchical bases, because they provide a natural environment for the implementation of a $p-$adaptation algorithm, see for example [56]. A central issue in finite element formulations for fluid problems is the choice of appropriate approximation spaces for the velocity and pressure variables (in the context of SWE, the role of the pressure is played by the free surface elevation). An inconsistent choice of the two approximation spaces indeed may result in a solution that is polluted by spurious modes, for the specific case of SWE see for example [31, 53, 54] as well as the more recent and comprehensive analysis in [30]. Here, we have not investigated this issue in depth, but the model implementation allows for approximations of higher polynomial degree p^u for the velocity fields than p^h for the height field. Even though no systematic study was performed, no significant differences were noticed between results obtained with equal or unequal degrees. In the following, only results with unequal degrees $p^u = p^h + 1$ are reported, with the exception of an empirical convergence test for a steady geostrophic flow.

All the integrals appearing in the elemental equations are evaluated by means of Gaussian numerical quadrature formulae, with a number of quadrature nodes consistent with the local polynomial degree being used. In particular, notice that integrals of terms in the image of the evolution operator E, i.e. of functions evaluated at the departure points of the trajectories arriving at the quadrature nodes, cannot be computed exactly (see e.g. [36, 40]), since such functions are not polynomials. Therefore a sufficiently accurate approximation of these integrals is needed, which may entail the need to employ numerical quadrature formulae with more nodes than the minimal requirement implied by the local polynomial degree. This overhead is actually compensated by the fact that, for each Gauss node, the computation

of the departure point is only to be executed once for all the quantities to be interpolated.

After spatial discretization has been performed, the discrete degrees of freedom representing velocity unknowns can be replaced in the respective discrete height equations, yielding in each case a linear system whose structure is entirely analogous to that obtained in [52]. The non-symmetric linear systems obtained from the TR-BDF2 stages are solved in our implementation by the GMRES method [46]. A classical stopping criterion based on a relative error tolerance of 10^{-10} was employed (see e.g. [24]). For the GMRES solver, so far, only a block diagonal preconditioning was employed. As it will be shown in section 7, the condition number of the systems to be solved can be greatly reduced if lower degree elements are employed close to the poles. In any case, the total computational cost of one TR-BDF2 step is entirely analogous to that of one step of the standard off centered trapezoidal rule employed in [52], since the structure of the systems is the same but for each stage only a fraction of the time step is being computed. Once h^{n+1} has been computed by solving this linear system, then $\mathbf{u}^{n+1}$ can be recovered by back substituting into the momentum equation.

6 Extension of the time integration approach to the Euler equations

In this section, we show that the previously proposed method can be extended seamlessly to the fully compressible Euler equations as formulated in equations (3) - (6). For simplicity, only the application to the (x, z) two dimensional vertical slice case is presented, but the extension to three dimensions is straightforward. Again, in order to avoid the solution of a nonlinear system, the dependency on Π in $\Pi\nabla\cdot\mathbf{u}$ and the dependency on Θ in $\Theta\nabla\pi$ are linearized in time, as common in semi-implicit discretizations based on the trapezoidal rule, see e.g. [10], [4].

The semi-Lagrangian counterpart of the TR substep of (8) is first applied to to (3) - (6), so as to obtain:

$$\begin{aligned}&\pi^{n+2\gamma}+\gamma\Delta t\ \left(c_p/c_v-1\right)\Pi^n\nabla\cdot\mathbf{u}^{n+2\gamma}=-\pi^*\\&+E\left(t^n,2\gamma\Delta t\right)\left[\Pi-\gamma\Delta t\left(c_p/c_v-1\right)\Pi\ \nabla\cdot\mathbf{u}\right],\end{aligned}\tag{19}$$

$$u^{n+2\gamma} + \gamma\Delta t\, c_p\Theta^n \frac{\partial \pi}{\partial x}^{n+2\gamma} = E(t^n, 2\gamma\Delta t)\left[u - \gamma\Delta t\, c_p\Theta\frac{\partial \pi}{\partial x}\right], \tag{20}$$

$$w^{n+2\gamma} + \gamma\Delta t\left(c_p\Theta^n \frac{\partial \pi}{\partial z}^{n+2\gamma} - g\frac{\theta^{n+2\gamma}}{\theta^*}\right) = E(t^n, 2\gamma\Delta t)\left[w - \gamma\Delta t\left(c_p\Theta\frac{\partial \pi}{\partial z} - g\frac{\theta}{\theta^*}\right)\right], \tag{21}$$

$$\theta^{n+2\gamma} + \gamma\Delta t\frac{d\theta^*}{dz}w^{n+2\gamma} = E(t^n, 2\gamma\Delta t)\left[\theta - \gamma\Delta t\frac{d\theta^*}{dz}w\right]. \tag{22}$$

Following [10] the time semi-discrete energy equation (22) can be inserted into the time semi-discrete vertical momentum equation (21), in order to decouple the momentum and the energy equations as follows

$$\begin{aligned}\left(1 + (\gamma\Delta t)^2\frac{g}{\theta^*}\frac{d\theta^*}{dz}\right)w^{n+2\gamma} + \gamma\Delta t c_p\Theta^n\frac{\partial \pi}{\partial z}^{n+2\gamma} &= \\ E(t^n, 2\gamma\Delta t)\left[w - \gamma\Delta t\left(c_p\Theta\frac{\partial \pi}{\partial z} - g\frac{\theta}{\theta^*}\right)\right] &\\ +\gamma\Delta t\frac{g}{\theta^*}E(t^n, 2\gamma\Delta t)\left[\theta - \gamma\Delta t\frac{d\theta^*}{dz}w\right]. &\end{aligned} \tag{23}$$

Equations (19), (20) and (23) are a set of three equations in three unknowns only, namely π, u, and w that can be compared with equations (15), (16) with $f = 0$ and $m_x = m_y = 1$ (Cartesian geometry). From the comparison it is clear that the two formulations are isomorphic under correspondence $\pi \longleftrightarrow h, u \longleftrightarrow u, w \longleftrightarrow v$.

We can then consider the semi-Lagrangian counterpart of the BDF2 substep of (8) applied to (3) - (6) to obtain:

$$\begin{aligned}\pi^{n+1} &+ \gamma_2\Delta t\,(c_p/c_v - 1)\,\Pi^{n+2\gamma}\nabla\cdot\mathbf{u}^{n+1} \\ &= -\pi^* + (1-\gamma_3)[E\,(t^n, \Delta t)\,\Pi] \\ &+ \gamma_3[E\,(t^n + 2\gamma\Delta t, (1-2\gamma)\Delta t)\,\Pi],\end{aligned} \tag{24}$$

$$
\begin{aligned}
u^{n+1} &+ \gamma_2 \Delta t \; c_p \Theta^{n+2\gamma} \frac{\partial \pi}{\partial x}^{n+1} \\
&= (1-\gamma_3)[E\,(t^n, \Delta t)\, u] \\
&+ \gamma_3 [E\,(t^n + 2\gamma\Delta t, (1-2\gamma)\Delta t)\, u], \qquad (25)
\end{aligned}
$$

$$
\begin{aligned}
w^{n+1} &+ \gamma_2 \Delta t \left(c_p \Theta^{n+2\gamma} \frac{\partial \pi}{\partial z}^{n+1} - g \frac{\theta^{n+1}}{\theta^*} \right) \\
&= (1-\gamma_3)[E\,(t^n, \Delta t)\, w] \\
&+ \gamma_3 [E\,(t^n + 2\gamma\Delta t, (1-2\gamma)\Delta t)\, w], \qquad (26)
\end{aligned}
$$

$$
\begin{aligned}
\theta^{n+1} &+ \gamma_2 \Delta t \frac{d\theta^*}{dz} w^{n+1} \\
&= (1-\gamma_3)[E\,(t^n, \Delta t)\, \theta] \\
&+ \gamma_3 [E\,(t^n + 2\gamma\Delta t, (1-2\gamma)\Delta t)\, \theta]. \qquad (27)
\end{aligned}
$$

Again, following [10], the time semi-discrete energy equation (27) can be inserted into the time semi-discrete vertical momentum equation (26), in order to decouple the momentum and the energy equations:

$$
\begin{aligned}
&\left(1 + (\gamma_2 \Delta t)^2 \frac{g}{\theta^*} \frac{d\theta^*}{dz}\right) w^{n+1} + \gamma_2 \Delta t \; c_p \Theta^{n+2\gamma} \frac{\partial \pi}{\partial z}^{n+1} = \\
&(1-\gamma_3)[E\,(t^n, \Delta t)\, w] + \gamma_3 [E\,(t^n + 2\gamma\Delta t, (1-2\gamma)\Delta t)\, w] + \qquad (28) \\
&\gamma_2 \Delta t \frac{g}{\theta^*} \left\{ (1-\gamma_3)[E\,(t^n, \Delta t)\, \theta] + \gamma_3 [E\,(t^n + 2\gamma\Delta t, (1-2\gamma)\Delta t)\, \theta] \right\}.
\end{aligned}
$$

Now equations (24), (25) and (28) are a set of three equations in three unknowns only, namely π, u, and w, that can be compared with equations (17), (18) with $f = 0$ and $m_x = m_y = 1$ (Cartesian geometry). Again, it is easy to see that also in this case exactly the same structure results as in equations (17)-(18) with the correspondence $\pi \longleftrightarrow h, u \longleftrightarrow u, w \longleftrightarrow v$, so that the approach (and code) proposed for the shallow water equations can be extended to the fully compressible Euler equation in a straightforward way.

7 Numerical experiments

The numerical method introduced in section 5 has been implemented and tested on a number of relevant test cases using different initial conditions and bathymetry profiles, in order to assess its accuracy and stability properties and to analyze the impact of the $p-$adaptivity strategy. Whenever a reference solution was available, the relative errors were computed in the L^1, L^2 and L^∞ norms at the final time t_f of the simulation according to [55] as:

$$l_1(h) = \frac{I\,[\,|h(\cdot,t_f) - h_{ref}(\cdot,t_f)|\,]}{I\,[\,|h_{ref}(\cdot,t_f)|\,]}, \tag{29}$$

$$l_2(h) = \frac{\left\{ I\Big[\,\big(\,h(\cdot,t_f) - h_{ref}(\cdot,t_f)\,\big)^2\,\Big]\right\}^{1/2}}{\left\{ I\big[\,h_{ref}(\cdot,t_f)^2\,\big]\right\}^{1/2}}, \tag{30}$$

$$l_\infty(h) = \frac{\max\,|h(\cdot,t_f) - h_{ref}(\cdot,t_f)|}{\max\,|h_{ref}(\cdot,t_f)|}, \tag{31}$$

where h_{ref} denotes the reference solution for a model variable h and I is a discrete approximation of the global integral

$$I(h) = \frac{\int_\Omega h\, m_x m_y\, d\mathbf{x}}{\int_\Omega m_x m_y\, d\mathbf{x}}, \tag{32}$$

computed by an appropriate numerical quadrature rule, consistent with the numerical approximation being tested, and the maximum is computed over all nodal values.

The test cases considered for the shallow water equations in spherical geometry are

- a steady-state geostrophic flow: in particular, we have analyzed results in test case 2 of [55] in the configuration least favorable for methods employing longitude-latitude meshes;
- the unsteady flow with exact analytical solution described in [29];
- the polar rotating low-high, introduced in [33], aimed at showing that no problems arise even in the case of strong cross polar flows;
- zonal flow over an isolated mountain and Rossby-Haurwitz wave of wavenumber 4, corresponding respectively to test cases 5 and 6 in [55].

For the first two tests, analytic solutions are available and empirical convergence tests can be performed. The test cases considered for the discretization of equations (3)-(6) are

- inertia gravity waves involving the evolution of a potential temperature perturbation in a channel with periodic boundary conditions and uniformly stratified environment with constant Brunt-Wäisälä frequency, as described in [47];
- a rising thermal bubble given by the evolution of a warm bubble in a constant potential temperature environment, as described in [23].

In all the numerical experiments performed for this paper, neither spectral filtering nor explicit diffusion of any kind were employed, the only numerical diffusion being implicit in the time discretization approach. We have not yet investigated to which extent the quality of the solutions is affected by this choice, but this should be taken into account when comparing quantitatively the results of the present method to those of reference models, such as the one described in [22], in which explicit numerical diffusion is added. Sensitivity of the comparison results to the amount of numerical diffusion has been highlighted in several model validation exercises, see e.g. [43].

Since semi-implicit, semi-Lagrangian methods are most efficient for low Froude number flows, where the typical velocity is much smaller than that of the fastest propagating waves, all the tests considered fall in this hydrodynamical regime. Therefore, in order to assess the method efficiency, a distinction has been made between the maximum Courant number based on the velocity, on one hand, and, on the other hand, the maximum Courant number based on the celerity, or the maximum Courant number based on the sound speed, defined respectively as

$$C_{vel} = \max \frac{\|\mathbf{u}\|_\infty \Delta t}{\Delta x/p}$$

$$C_{cel} = \max \frac{\sqrt{gh}\Delta t}{\Delta x/p}, \quad C_{snd} = \max \frac{\sqrt{(c_p/c_v)R\Theta\Pi}\Delta t}{\Delta x/p},$$

where Δx is to be interpreted as generic value of the meshsize in either coordinate direction. For the tests in which $p-$adaptivity was employed, if p_I^n denotes the local polynomial degree used at timestep t^n to represent a model variable inside the $I-th$ element of the mesh, while p_{max} is the maximum local polynomial degree considered, the efficiency of the method in reducing the computational effort has been measured by monitoring the evolution of the quantities

$$\Delta_{dof}^n = \frac{\sum_{I=1}^N (p_I^n+1)^2}{N(p_{max}+1)^2}, \qquad \Delta_{iter}^n = \frac{\mathrm{ITN}_{adapt}^n}{\mathrm{ITN}_{max}^n},$$

where N is the total number of elements, ITN_{adapt}^n denotes the total number of GMRES iterations at time step n for the adapted local

degrees configuration and ITN^n_{max} the total number of GMRES iterations at time step n for the configuration with maximum degree in all elements, respectively. Average values of these indicators over the simulations performed are reported in the following, denoted by $\Delta^{average}_{dof}$ and $\Delta^{average}_{iter}$ respectively. The error between the adaptive solution and the corresponding one obtained with uniform maximum polynomial degree everywhere has been measured in terms of (29). Finally, in some cases conservation of global invariants has been monitored by evaluating at each time step the following global integral quantities:

$$J(q^n) = \frac{I(q(\cdot, t^n)) - I(q(\cdot, t^0))}{I(q(\cdot, t^0))}, \tag{33}$$

where $I(q)$ has been defined in (32) and $q^n = q(\cdot, t^n)$ is the density associated to each global invariant. According to the choice of q, following invariants are considered: mass, i.e. $q = q_{mass} = h$, total energy, i.e. $q = q_{energ} = \frac{1}{2}(h\boldsymbol{u}\cdot\boldsymbol{u} + g(h^2 - b^2))$, and potential enstrophy, i.e. $q = q_{enstr} = \frac{1}{2h}(\hat{\boldsymbol{k}} \cdot \nabla \times \boldsymbol{u} + f)^2$.

7.1 Steady-state geostrophic flow

We first consider the test case 2 of [55], where the solution is a steady state flow with velocity field corresponding to a zonal solid body rotation and h field obtained from the velocity ones through geostrophic balance. All the parameter values are taken as in [55]. The flow orientation parameter has been chosen here as $\alpha = \pi/2 - 0.05$, making the test more challenging on a longitute-latitude mesh. Error norms associated to the solution obtained on a mesh of 10×5 elements for different polynomial degrees are shown in tables 1, 2 and 3 for h, u and v, respectively. All the results have been computed at $t_f = 10$ days at fixed maximum Courant numbers $C_{cel} = 8, C_{vel} = 2$, so that different values of Δt have been employed for different polynomial order. We remark that the resulting time steps are significantly larger than those allowed by typical explicit time discretizations for analogous DG space discretizations, see e.g. the results in [38]. The spectral decay in the error norms can be clearly observed, until the time error becomes dominant. For better comparison with the results in [38], we consider again the configuration with $p^h = 6, p^u = 7$ on 10×5 elements, which corresponds to the same resolution in space as for the $150 \times 8 \times 8$ grid used in [38]. While $\Delta t = 36$ s is used in [38] giving a $l_\infty(h) \approx 8 \times 10^{-6}$, the proposed SISLDG formulation can be run with $\Delta t = 3600$ s, in which case $l_\infty(h) \approx 3 \times 10^{-7}$, and the average number of iterations

required by the linear solver is 1 for the TR substep and 4 for the BDF2 substep.

p^h	p^u	Δt $[s]$	$l_1(h)$	$l_2(h)$	$l_\infty(h)$
2	3	4800	5.558×10^{-3}	6.805×10^{-3}	1.914×10^{-2}
3	4	3600	6.017×10^{-4}	8.176×10^{-4}	2.569×10^{-3}
4	5	2880	1.743×10^{-5}	2.405×10^{-5}	9.024×10^{-5}
5	6	2400	1.586×10^{-6}	2.281×10^{-6}	1.058×10^{-5}
6	7	2057	8.829×10^{-8}	1.206×10^{-7}	4.926×10^{-7}
7	8	1800	1.246×10^{-8}	1.590×10^{-8}	4.158×10^{-8}
8	9	1600	5.641×10^{-9}	5.952×10^{-9}	6.320×10^{-9}

Table 1: Relative errors on h for different polynomial degrees, SWE test case 2 with $\alpha = \pi/2 - 0.05$ at time $t_f = 10$ days.

p^h	p^u	Δt $[s]$	$l_1(u)$	$l_2(u)$	$l_\infty(u)$
2	3	4800	6.351×10^{-2}	6.432×10^{-2}	1.143×10^{-1}
3	4	3600	9.505×10^{-3}	1.037×10^{-2}	2.106×10^{-2}
4	5	2880	4.288×10^{-4}	4.887×10^{-4}	2.393×10^{-3}
5	6	2400	4.598×10^{-5}	4.830×10^{-5}	1.706×10^{-4}
6	7	2057	2.057×10^{-6}	2.262×10^{-6}	5.879×10^{-6}
7	8	1800	2.162×10^{-7}	2.358×10^{-7}	6.428×10^{-7}
8	9	1600	2.013×10^{-8}	2.276×10^{-8}	3.268×10^{-8}

Table 2: Relative errors on u for different polynomial degrees, SWE test case 2 with $\alpha = \pi/2 - 0.05$ at time $t_f = 10$ days.

Another convergence test was performed for $p^h = p^u = 3$, increasing the number of elements and correspondingly decreasing the value of the time step. In this case, the maximum Courant numbers vary because of the mesh inhomogeneity, so that $2 < C_{cel} < 18$, $0.5 < C_{vel} < 4$. The results are reported in tables 4, 5 and 6 for h, u and v, respectively. The empirical convergence order q_2^{emp} based on the l_2 norm errors has also been estimated, showing that in this stationary test convergence rates above the second order of the time discretization can be achieved.

p^h	p^u	Δt $[s]$	$l_1(v)$	$l_2(v)$	$l_\infty(v)$
2	3	4800	1.001×10^{-1}	1.016×10^{-1}	2.698×10^{-1}
3	4	3600	1.859×10^{-2}	1.823×10^{-2}	6.848×10^{-2}
4	5	2880	7.376×10^{-4}	7.428×10^{-4}	2.884×10^{-3}
5	6	2400	8.185×10^{-5}	8.307×10^{-5}	2.574×10^{-4}
6	7	2057	3.074×10^{-6}	3.173×10^{-6}	1.123×10^{-5}
7	8	1800	3.370×10^{-7}	3.432×10^{-7}	1.323×10^{-6}
8	9	1600	2.175×10^{-8}	2.317×10^{-8}	5.124×10^{-8}

Table 3: Relative errors on v for different polynomial degrees, SWE test case 2 with $\alpha = \pi/2 - 0.05$ at time $t_f = 10$ days.

$N_x \times N_y$	Δt $[s]$	$l_1(h)$	$l_2(h)$	$l_\infty(h)$	q_2^{emp}
10×5	3600	2.557×10^{-4}	3.495×10^{-4}	1.403×10^{-3}	–
20×10	1800	2.187×10^{-5}	2.889×10^{-5}	1.566×10^{-4}	3.6
40×20	900	2.530×10^{-6}	3.353×10^{-6}	1.430×10^{-5}	3.1
80×40	450	3.996×10^{-7}	5.534×10^{-7}	3.134×10^{-6}	2.6

Table 4: Relative errors on h for different number of elements, $p^h = p^u = 3$, SWE test case 2 with $\alpha = \pi/2 - 0.05$ at time $t_f = 10$ days.

$N_x \times N_y$	Δt $[s]$	$l_1(u)$	$l_2(u)$	$l_\infty(u)$	q_2^{emp}
10×5	3600	2.769×10^{-3}	3.358×10^{-3}	8.948×10^{-3}	–
20×10	1800	2.896×10^{-4}	3.720×10^{-4}	2.414×10^{-3}	3.2
40×20	900	3.647×10^{-5}	4.563×10^{-5}	2.473×10^{-4}	3.0
80×40	450	6.826×10^{-6}	1.035×10^{-5}	9.525×10^{-5}	2.1

Table 5: Relative errors on u for different number of elements, $p^h = p^u = 3$, SWE test case 2 with $\alpha = \pi/2 - 0.05$ at time $t_f = 10$ days.

$N_x \times N_y$	Δt $[s]$	$l_1(v)$	$l_2(v)$	$l_\infty(v)$	q_2^{emp}
10×5	3600	3.309×10^{-3}	3.346×10^{-3}	8.250×10^{-3}	–
20×10	1800	4.016×10^{-4}	4.233×10^{-4}	1.255×10^{-3}	3.0
40×20	900	5.180×10^{-5}	5.578×10^{-5}	2.329×10^{-4}	2.9
80×40	450	9.405×10^{-6}	1.214×10^{-5}	7.763×10^{-5}	2.2

Table 6: Relative errors on v for different number of elements, $p^h = p^u = 3$, SWE test case 2 with $\alpha = \pi/2 - 0.05$ at time $t_f = 10$ days.

7.2 Unsteady flow with analytic solution

In a second, time dependent test, the analytic solution of (1)-(2) derived in [29] has been employed to assess the performance of the proposed discretization. More specifically, the analytic solution defined in formula (23) of [29] was used. Since the exact solution is periodic, the initial profiles also correspond to the exact solution an integer number of days later. The proposed SISLDG scheme has been integrated up to $t_f = 5$ days with $p^h = 4$ and $p^u = 5$ on meshes with increasing number of elements, while the time step has been decreased accordingly. In this case, the maximum Courant numbers vary because of the mesh dishomogeneity, so that $4 < C_{cel} < 26$, $1.25 < C_{vel} < 8$. Error norms for h, u, v of the above-mentioned integrations have been computed at $t_f = 5$ days and displayed in tables 7 - 9. An empirical order estimation shows that full second order accuracy in time is attained.

$N_x \times N_y$	Δt $[s]$	$l_1(h)$	$l_2(h)$	$l_\infty(h)$	q_2^{emp}
10×5	3600	5.456×10^{-3}	6.120×10^{-3}	9.537×10^{-3}	-
20×10	1800	1.246×10^{-3}	1.397×10^{-3}	2.143×10^{-3}	2.1
40×20	900	3.039×10^{-4}	3.410×10^{-4}	5.207×10^{-4}	2.0
80×40	450	7.548×10^{-5}	8.475×10^{-5}	1.292×10^{-4}	2.0

Table 7: Relative errors on h at different resolutions, Läuter test case.

$N_x \times N_y$	Δt $[s]$	$l_1(u)$	$l_2(u)$	$l_\infty(u)$	q_2^{emp}
10×5	3600	6.567×10^{-2}	7.848×10^{-2}	1.670×10^{-1}	-
20×10	1800	1.665×10^{-2}	1.994×10^{-2}	3.931×10^{-2}	2.0
40×20	900	4.210×10^{-3}	5.032×10^{-3}	9.811×10^{-3}	2.0
80×40	450	1.057×10^{-3}	1.261×10^{-3}	2.452×10^{-3}	2.0

Table 8: Relative errors on u at different resolutions, Läuter test case.

For comparison, analogous errors have been computed with the same discretization parameters but employing the off centered Crank Nicolson method of [52] with $\theta = 0.6$. The resulting improvement in the errors between the TRBDF2 scheme and the off-centered Crank Nicolson is achieved at an essentially equivalent computational cost in terms of total CPU time employed.

$N_x \times N_y$	Δt $[s]$	$l_1(v)$	$l_2(v)$	$l_\infty(v)$	q_2^{emp}
10×5	3600	1.174×10^{-1}	1.198×10^{-1}	2.316×10^{-1}	-
20×10	1800	2.939×10^{-2}	3.002×10^{-2}	5.561×10^{-2}	2.0
40×20	900	7.336×10^{-3}	7.497×10^{-3}	1.390×10^{-2}	2.0
80×40	450	1.833×10^{-3}	1.874×10^{-3}	3.464×10^{-3}	2.0

Table 9: Relative errors on v at different resolutions, Läuter test case.

$N_x \times N_y$	Δt $[s]$	$l_1(h)$	$l_2(h)$	$l_\infty(h)$	q_2^{emp}
10×5	3600	1.444×10^{-2}	1.633×10^{-2}	2.398×10^{-2}	-
20×10	1800	8.742×10^{-3}	9.894×10^{-3}	1.445×10^{-2}	0.7
40×20	900	4.814×10^{-3}	5.451×10^{-3}	7.956×10^{-3}	0.9
80×40	450	2.526×10^{-3}	2.861×10^{-3}	4.177×10^{-3}	0.9

Table 10: Relative errors on h at different resolutions, Läuter test case with off centered Crank Nicolson, $\theta = 0.6$.

$N_x \times N_y$	Δt $[s]$	$l_1(u)$	$l_2(u)$	$l_\infty(u)$	q_2^{emp}
10×5	3600	1.800×10^{-1}	2.092×10^{-1}	3.810×10^{-1}	-
20×10	1800	1.077×10^{-1}	1.255×10^{-1}	2.155×10^{-1}	0.7
40×20	900	5.895×10^{-2}	6.880×10^{-2}	1.186×10^{-1}	0.9
80×40	450	3.084×10^{-2}	3.603×10^{-2}	6.234×10^{-2}	0.9

Table 11: Relative errors on u at different resolutions, Läuter test case with off centered Crank Nicolson, $\theta = 0.6$.

$N_x \times N_y$	Δt $[s]$	$l_1(v)$	$l_2(v)$	$l_\infty(v)$	q_2^{emp}
10×5	3600	3.608×10^{-1}	3.665×10^{-1}	5.166×10^{-1}	-
20×10	1800	2.164×10^{-1}	2.198×10^{-1}	3.041×10^{-1}	0.7
40×20	900	1.185×10^{-1}	1.203×10^{-1}	1.671×10^{-2}	0.9
80×40	450	6.195×10^{-2}	6.291×10^{-2}	8.809×10^{-2}	0.9

Table 12: Relative errors on v at different resolutions, Läuter test case with off centered Crank Nicolson, $\theta = 0.6$.

7.3 Zonal flow over an isolated mountain

We have then performed numerical simulations reproducing the test case 5 of [55], given by a zonal flow impinging on an isolated mountain of conical shape. The geostrophic balance here is broken by orographic forcing, which results in the development of a planetary wave propagating all around the globe.

Plots of the fluid depth h as well as of the velocity components u and v at 15 days are shown in figures 6-8. The resolution used corresponds to a mesh of 60×30 elements with $p^h = 4$, $p^u = 5$, and $\Delta t = 900$ s, giving a Courant number $C_{cel} \approx 58$ in elements close to the poles. It can be observed that all the main features of the flow are correctly reproduced. In particular, no significant Gibbs phenomena are detected in the vicinity of the mountain, even in the initial stages of the simulation.

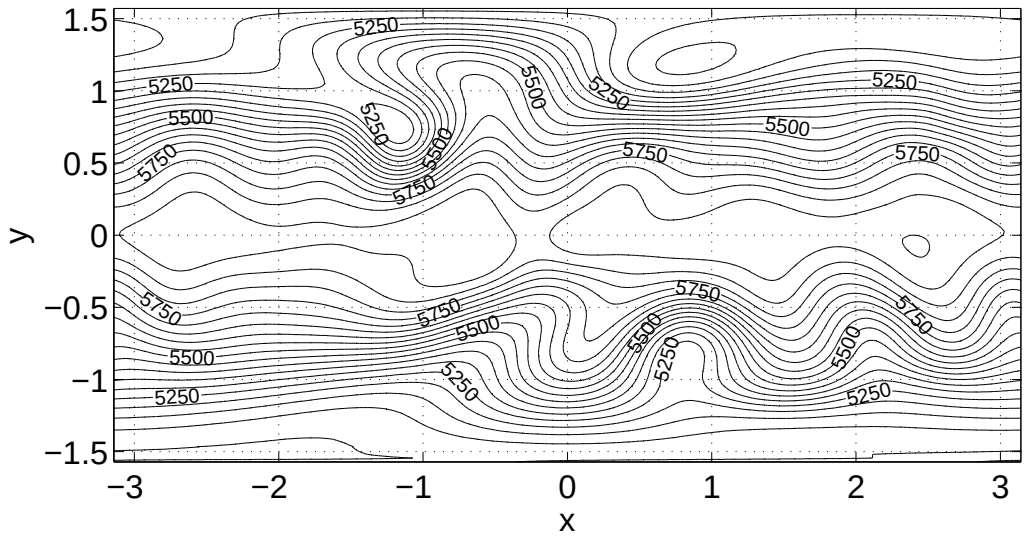

Figure 6: h field after 15 days, isolated mountain wave test case, $C_{cel} \approx 58$. Contour lines spacing is 50 m.

The evolution in time of global invariants during this simulation is shown in figures 9(a), 9(b), 9(c), respectively. Error norms for h and u at different resolutions corresponding to a $C_{cel} \approx 6$ and $p^h = p^u = 3$, have been computed at $t_f = 5$ days and are displayed in tables 13 - 14, with respect to a reference solution given by the National Center for Atmospheric Research (NCAR) spectral model [22] at resolution T511. It is apparent the second order of the proposed SISLDG scheme in time. Since, as observed in [22], the National Center for Atmospheric Research (NCAR) spectral model incorporates diffusion terms

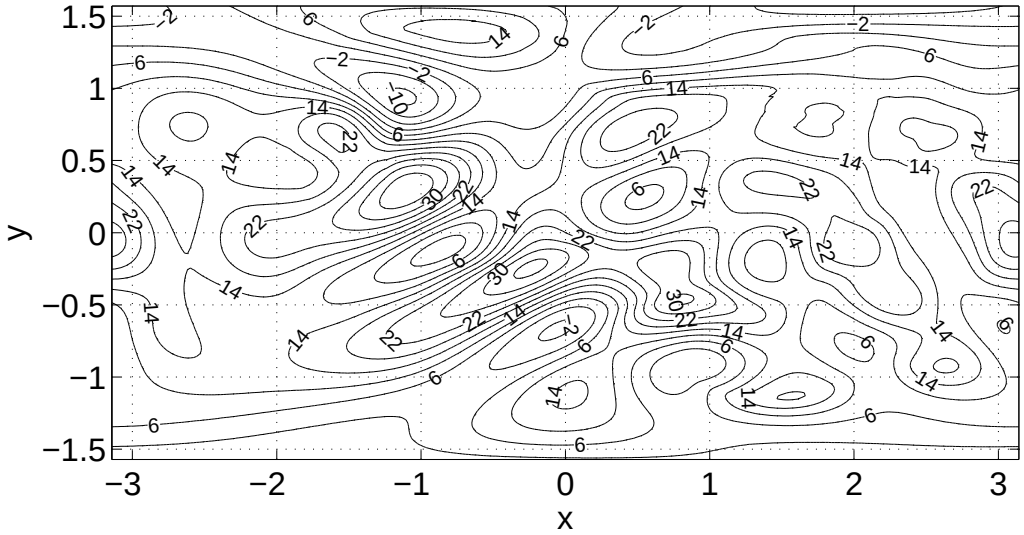

Figure 7: u field after 15 days, isolated mountain wave test case, $C_{cel} \approx 58$. Contour lines spacing is 4 m s^{-1}.

in the governing equations, while the proposed SISLDG scheme does not employ any diffusion terms nor filtering, nor smoothing of the topography, for this test it seemed more appropriate to compute relative errors with respect to NCAR spectral model [22] solution at an earlier time, $t_f = 5$ days, when it can be assumed that the effects of diffusion have less impact. Error norms for h and u have been computed at $t_f = 15$ days at different resolutions (corresponding to a $C_{cel} \approx 7$), $p^h = p^u = 3$, and displayed in tables 15 - 16.

$N_x \times N_y$	Δt[min]	$l_1(h)$	$l_2(h)$	$l_\infty(h)$	q_2^{emp}
12×6	20	8.19×10^{-4}	1.08×10^{-3}	5.90×10^{-3}	-
24×12	10	1.49×10^{-4}	2.08×10^{-4}	1.92×10^{-3}	2.4
48×24	5	2.88×10^{-5}	4.25×10^{-5}	8.40×10^{-4}	2.3

Table 13: Relative errors on h at different resolutions, isolated mountain wave test case, $t_f = 5$ days.

Finally the mountain wave test case has been run on the same mesh of 60×30 elements, $\Delta t = 900$ s, with either static or static plus dynamic adaptivity. The tolerance ϵ for the dynamic adaptivity [52] has been set to $\epsilon = 10^{-2}$. Results are reported in terms of error norms with respect to a nonadaptive solution at the maximum uniform

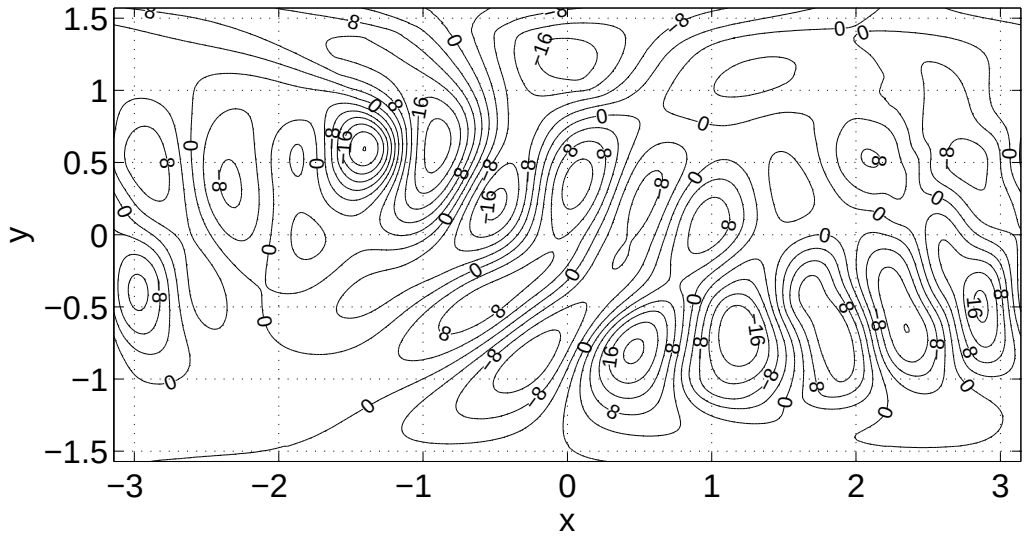

Figure 8: v field after 15 days, isolated mountain wave test case, $C_{cel} \approx 58$. Contour lines spacing is 4 m s^{-1}.

$N_x \times N_y$	Δt[min]	$l_1(u)$	$l_2(u)$	$l_\infty(u)$	q_2^{emp}
12×6	20	4.33×10^{-2}	5.81×10^{-2}	1.39×10^{-1}	-
24×12	10	5.70×10^{-3}	7.33×10^{-3}	1.06×10^{-1}	2.9
48×24	5	1.11×10^{-3}	1.72×10^{-3}	1.56×10^{-2}	2.2

Table 14: Relative errors on u at different resolutions, isolated mountain wave test case, $t_f = 5$ days.

resolution and in terms of efficiency gain, measured through the saving of number of linear solver iterations per time-step $\Delta_{iter}^{average}$ as well as through the saving of number of degrees of freedom actually used per timestep $\Delta_{dof}^{average}$; these results are summarized in tables 17 - 19: the use of static adaptivity only resulted in $\Delta_{iter}^{average} \approx 10.7\%$ and $\Delta_{dof}^{average} \approx 88\%$, while the use of both static and dynamic adaptivity led to $\Delta_{iter}^{average} \approx 13\%$ and $\Delta_{dof}^{average} \approx 45\%$. The distribution of the statically and dynamically adapted local polynomial degree used to represent the solution after 15 days is shown in figure 10. It can be noticed how, even after 15 days, higher polynomial degrees are still automatically concentrated around the location of the mountain.

$N_x \times N_y$	Δt[s]	$l_1(h)$	$l_2(h)$	$l_\infty(h)$	q_2^{emp}
12×6	1500	2.34×10^{-3}	2.92×10^{-3}	1.49×10^{-2}	-
24×12	750	5.99×10^{-4}	7.72×10^{-4}	3.87×10^{-3}	1.9
48×24	375	2.00×10^{-4}	2.74×10^{-4}	1.87×10^{-3}	1.5

Table 15: Relative errors on h at different resolutions, isolated mountain wave test case, $t_f = 15$ days.

$N_x \times N_y$	Δt[s]	$l_1(u)$	$l_2(u)$	$l_\infty(u)$	q_2^{emp}
12×6	1500	1.12×10^{-1}	1.29×10^{-1}	2.97×10^{-1}	-
24×12	750	2.09×10^{-2}	2.37×10^{-2}	5.73×10^{-2}	2.4
48×24	375	6.37×10^{-3}	7.92×10^{-3}	3.39×10^{-2}	1.6

Table 16: Relative errors on u at different resolutions, isolated mountain wave test case, $t_f = 15$ days.

adaptivity	$l_1(h)$	$l_2(h)$	$l_\infty(h)$
static	1.415×10^{-4}	3.314×10^{-4}	2.117×10^{-3}
static + dynamic	1.660×10^{-4}	3.419×10^{-4}	2.038×10^{-3}

Table 17: Relative errors between (statically and statically plus dynamically) adaptive and nonadaptive solution for isolated mountain wave test case, h field.

adaptivity	$l_1(u)$	$l_2(u)$	$l_\infty(u)$
static	1.289×10^{-2}	3.275×10^{-2}	1.524×10^{-1}
static + dynamic	1.509×10^{-2}	3.309×10^{-2}	1.475×10^{-1}

Table 18: Relative errors between (statically and statically plus dynamically) adaptive and nonadaptive solution for isolated mountain wave test case, u field.

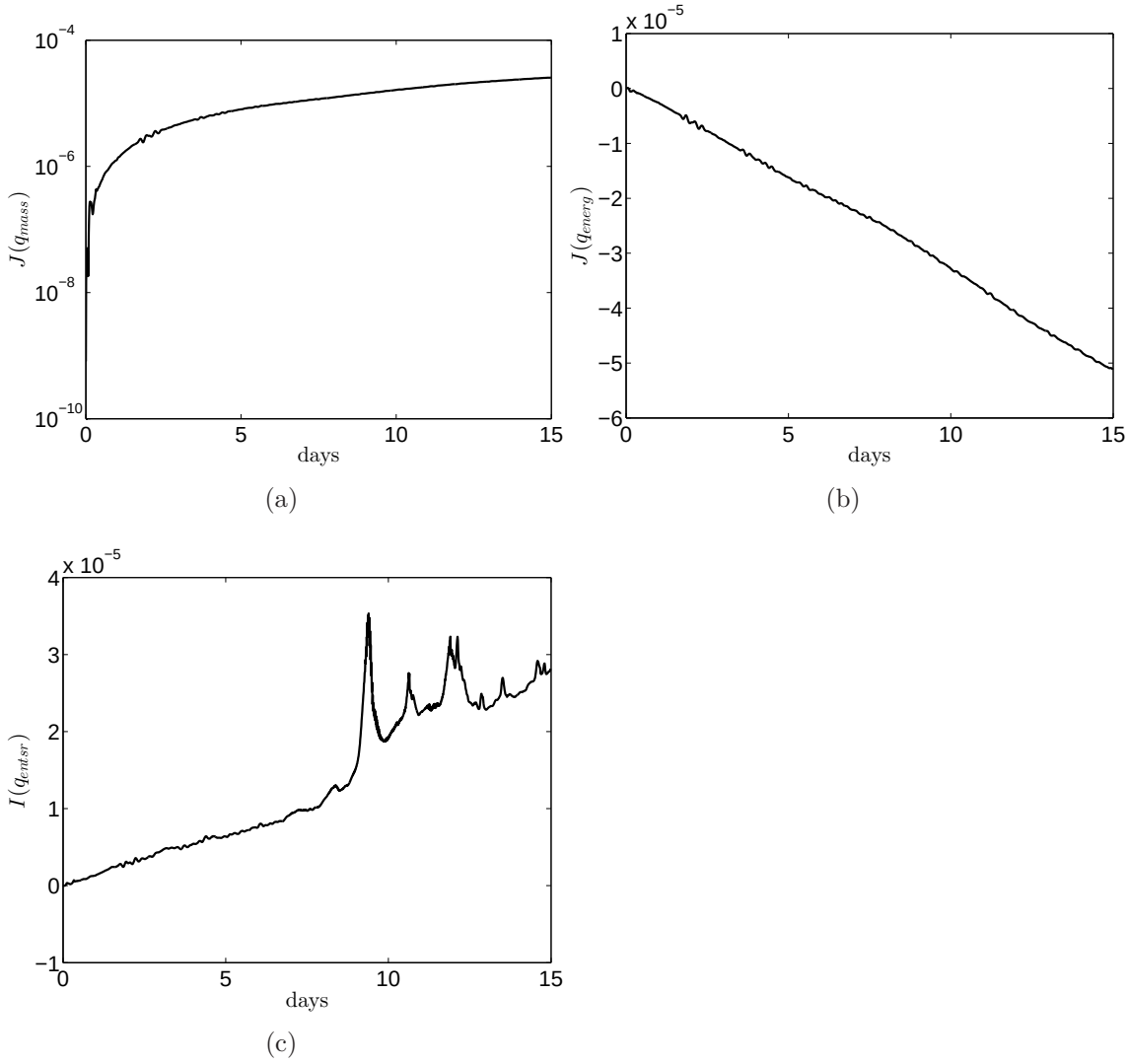

Figure 9: Integral invariants evolution, mass (a), energy (b), potential enstrophy (c), isolated mountain wave test case, $C_{cel} \approx 58$.

adaptivity	$l_1(v)$	$l_2(v)$	$l_\infty(v)$
static	2.501×10^{-2}	6.824×10^{-2}	6.597×10^{-1}
static + dynamic	2.833×10^{-2}	7.019×10^{-2}	6.975×10^{-1}

Table 19: Relative errors between (statically and statically plus dynamically) adaptive and nonadaptive solution for isolated mountain wave test case, v field.

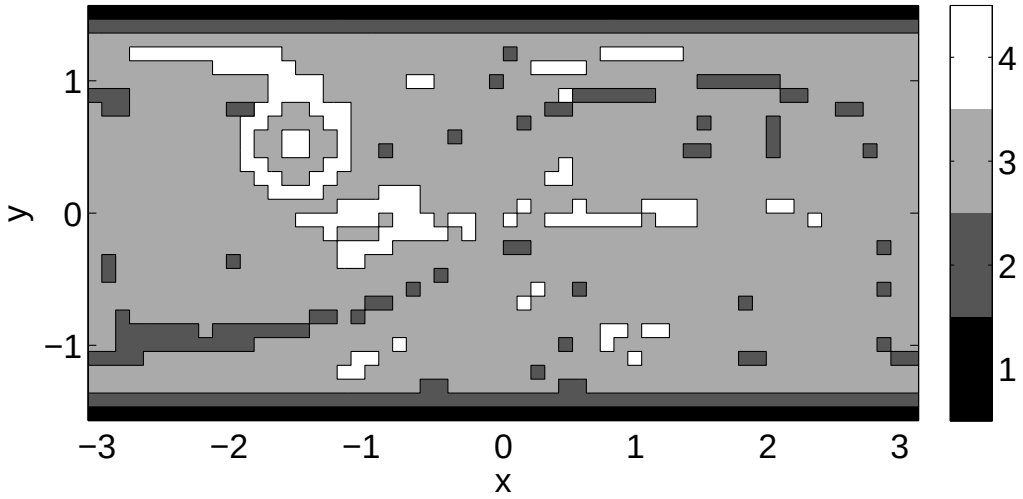

Figure 10: Statically and dynamically adapted local p^h distribution at 15 days, isolated mountain wave test case.

7.4 Rossby-Haurwitz wave

We have then considered test case 6 of [55], where the initial datum consists of a Rossby-Haurwitz wave of wave number 4. This case actually concerns a solution of the nondivergent barotropic vorticity equation, that is not an exact solution of the system (1) - (2). For a discussion about the stability of this profile as a solution of (1) - (2) see [50]. Plots of the fluid depth h as well as of the velocity components u and v at 15 days are shown in figures 11-13. The resolution used corresponds to a mesh of 64×32 elements with $p^h = 4$, $p^u = 5$, and $\Delta t = 900$ s, giving a Courant number $C_{cel} \approx 83$ in elements close to poles. It can be observed that all the main features of the flow are correctly reproduced.

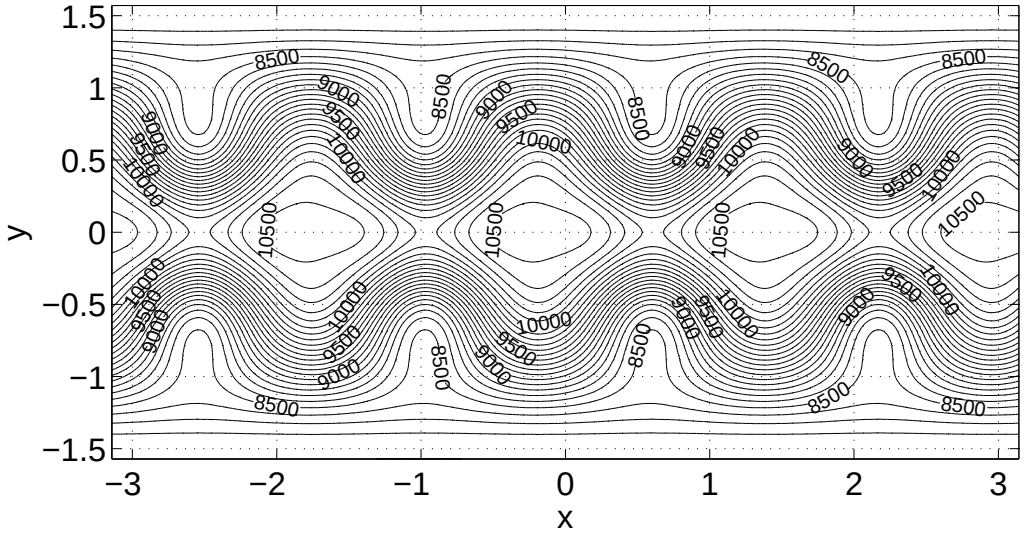

Figure 11: h field after 15 days, Rossby-Haurwitz wave test case, $C_{cel} \approx 83$. Contour lines spacing is 100 m.

The evolution in time of global invariants during this simulation is shown in figures 14(a), 14(b), 14(c), respectively. Error norms for h and u at different resolutions, corresponding to a $C_{cel} \approx 32$ and $p^h = 4, p^u = 5$ have been computed at $t_f = 15$ days and are displayed in tables 20 - 21, with respect to a reference solution given by the National Center for Atmospheric Research (NCAR) spectral model [22] at resolution T511. It is apparent the second order of the proposed SISLDG scheme in time. Unlike the NCAR spectral model, the proposed SISLDG scheme does not employ any explicit numerical diffusion.

Finally, the Rossby-Haurwitz wave test case has been run on the

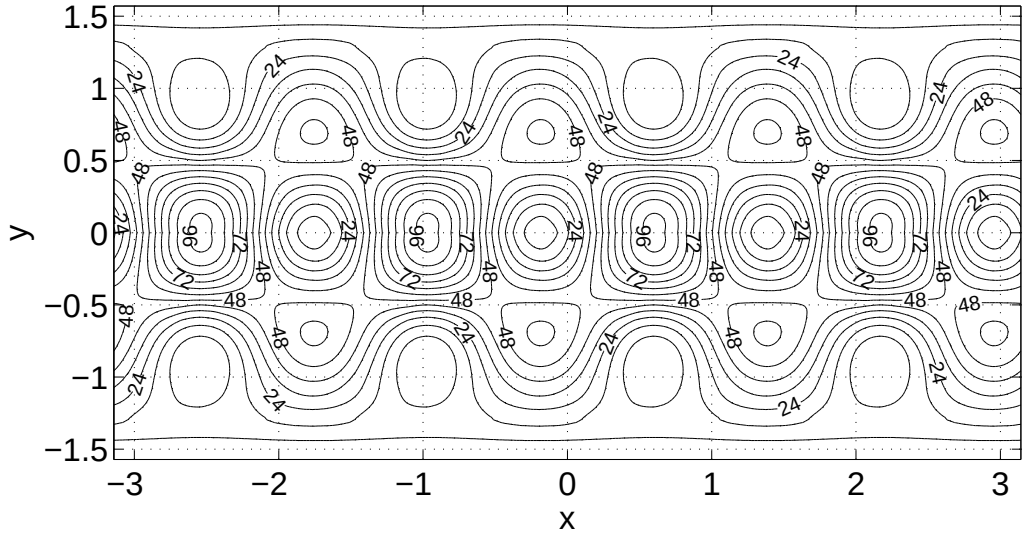

Figure 12: u field after 15 days, Rossby-Haurwitz wave test case, $C_{cel} \approx 83$. Contour lines spacing is 8 m s^{-1}.

$N_x \times N_y$	Δt[min]	$l_1(h)$	$l_2(h)$	$l_\infty(h)$	q_2^{emp}
10×5	60	2.92×10^{-2}	3.82×10^{-2}	6.75×10^{-2}	-
20×10	30	5.50×10^{-3}	6.80×10^{-3}	1.11×10^{-2}	2.4
40×20	15	1.40×10^{-3}	1.80×10^{-3}	3.20×10^{-3}	2.0

Table 20: Relative errors on h at different resolutions, Rossby-Haurwitz wave test case.

same mesh of 64×32 elements, $\Delta t = 900$ s, with either static or static plus dynamic adaptivity. The tolerance ϵ for the dynamic adaptivity [52] has been set to $\epsilon = 5 \times 10^{-2}$. Results are reported in terms of error norms with respect to a nonadaptive solution at the maximum uniform resolution and in terms of efficiency gain, measured through the saving of number of linear solver iterations per time-step $\Delta_{iter}^{average}$ as well as through the saving of number of degrees of freedom actually used per timestep $\Delta_{dof}^{average}$; these results are summarized in tables 22 - 24: the use of static adaptivity only resulted in $\Delta_{iter}^{average} \approx 10.7\%$ and $\Delta_{dof}^{average} \approx 88\%$, while the use of both static and dynamic adaptivity led to $\Delta_{iter}^{average} \approx 13\%$ and $\Delta_{dof}^{average} \approx 45\%$. The distribution of the statically and dynamically adapted local polynomial degree used to represent the solution after 15 days is shown in figure 15. It can be noticed how, even after 15 days, and even if the maximum allowed p^h

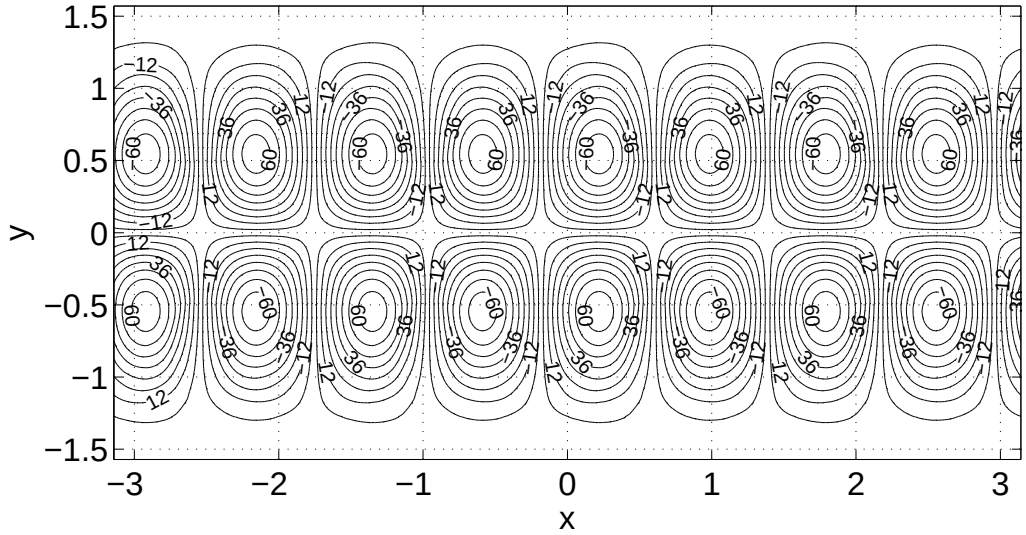

Figure 13: v field after 15 days, Rossby-Haurwitz wave test case, $C_{cel} \approx 83$. Contour lines spacing is 8 m s^{-1}.

$N_x \times N_y$	Δt[min]	$l_1(u)$	$l_2(u)$	$l_\infty(u)$	q_2^{emp}
10×5	60	4.065×10^{-1}	3.775×10^{-1}	2.305×10^{-1}	-
20×10	30	7.79×10^{-2}	7.33×10^{-2}	5.67×10^{-2}	2.4
40×20	15	2.04×10^{-2}	1.95×10^{-2}	1.76×10^{-2}	1.9

Table 21: Relative errors on u at different resolutions, Rossby-Haurwitz wave test case.

is 4, the use of the adaptivity criterion with $\epsilon = 5 \times 10^{-2}$ leads to the use of at most cubic polynomials for the local representation of h.

adaptivity	$l_1(h)$	$l_2(h)$	$l_\infty(h)$
static	2.182×10^{-4}	3.434×10^{-4}	2.856×10^{-4}
static + dynamic	2.358×10^{-3}	2.963×10^{-3}	5.157×10^{-3}

Table 22: Relative errors between (statically and statically plus dynamically) adaptive and nonadaptive solution for Rossby-Haurwitz wave test case, h field.

adaptivity	$l_1(u)$	$l_2(u)$	$l_\infty(u)$
static	7.041×10^{-3}	1.236×10^{-2}	2.834×10^{-2}
static + dynamic	3.639×10^{-2}	3.387×10^{-2}	2.678×10^{-2}

Table 23: Relative errors between (statically and statically plus dynamically) adaptive and nonadaptive solution for Rossby-Haurwitz wave test case, u field.

adaptivity	$l_1(v)$	$l_2(v)$	$l_\infty(v)$
static	3.158×10^{-3}	3.250×10^{-3}	1.148×10^{-2}
static + dynamic	2.723×10^{-2}	2.432×10^{-2}	2.646×10^{-2}

Table 24: Relative errors between (statically and statically plus dynamically) adaptive and nonadaptive solution for Rossby-Haurwitz wave test case, v field.

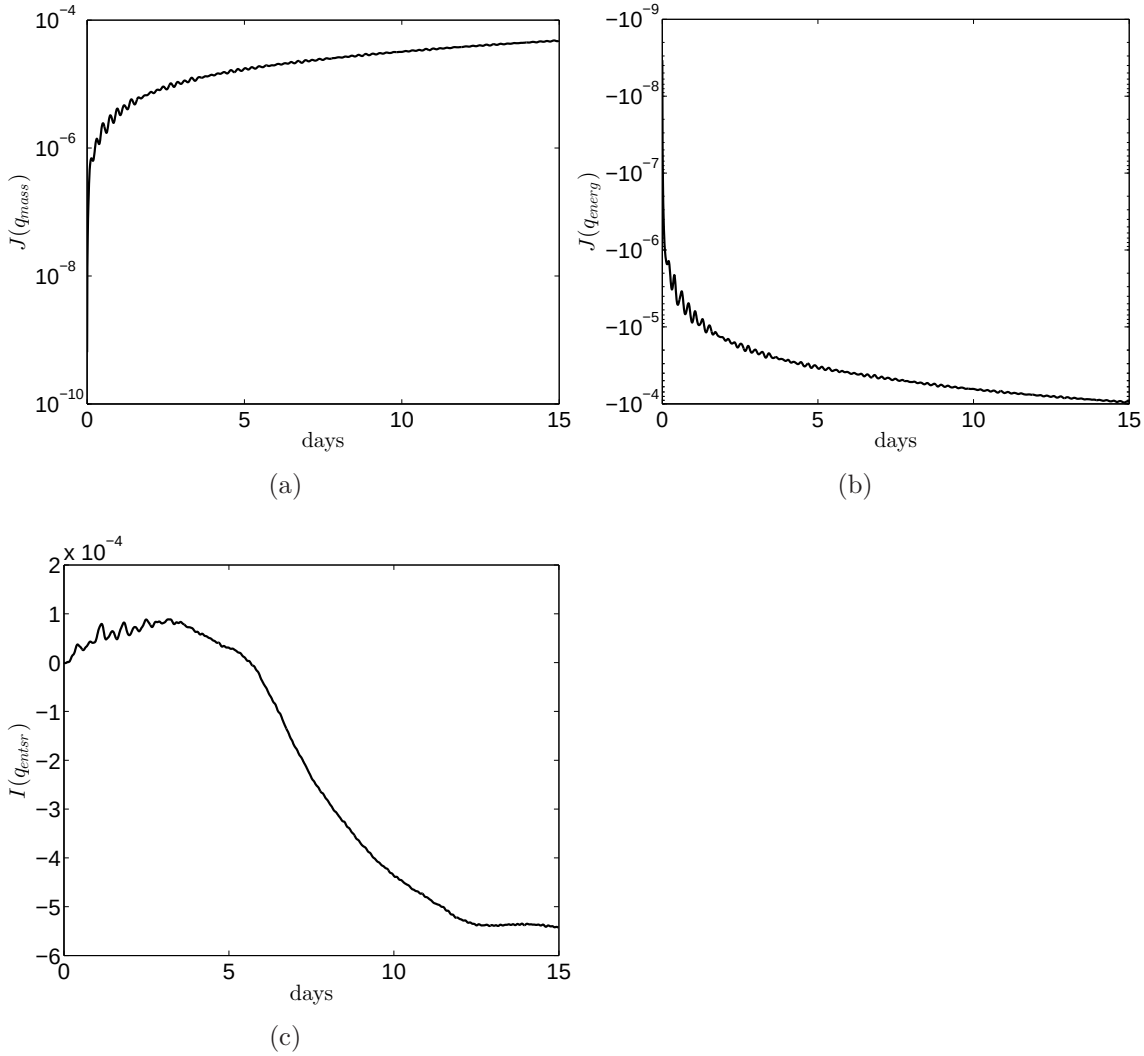

Figure 14: Integral invariants evolution, mass (a), energy (b), potential enstrophy (c), Rossby-Haurwitz wave test case, $C_{cel} \approx 83$.

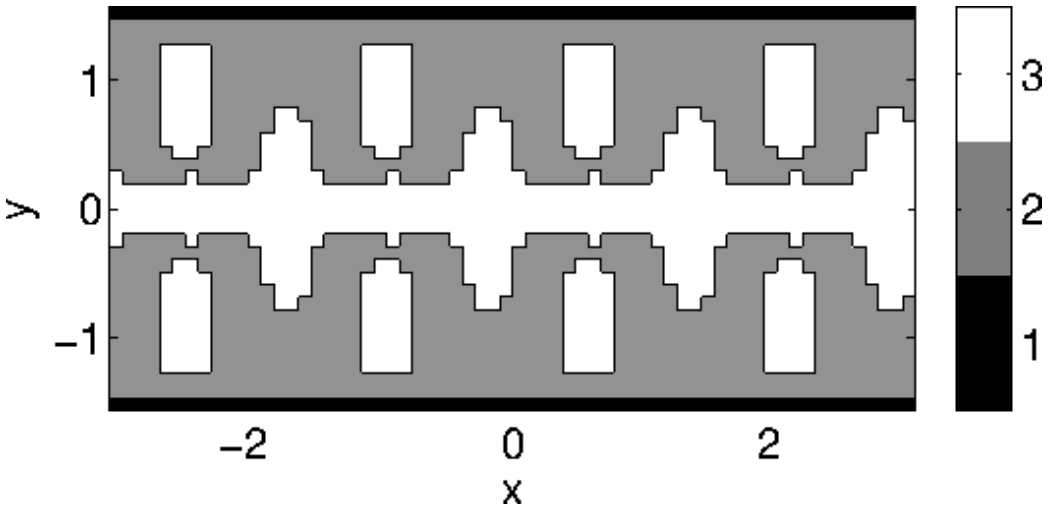

Figure 15: Statically and dynamically adapted local p^h distribution at 15 days, Rossby-Haurwitz test case.

7.5 Nonhydrostatic inertia gravity waves

In this section we consider the test case proposed in [47]. It consists in a set of inertia-gravity waves propagating in a channel with a uniformly stratified reference atmosphere characterized by a constant Brunt-Wäisälä frequency $N^2 = 0.01$. The domain and the initial and boundary conditions are identical to those of [47]. The initial perturbation in potential temperature radiates symmetrically to the left and to the right, but because of the superimposed mean horizontal flow ($u = 20$m/s), does not remain centered around the initial position. Contours of potential temperature perturbation, horizontal velocity, and vertical velocity time $t_f = 3000$ s are shown in figures 16, 17, 18, respectively. The computed results compare well with the structure displayed by the analytical solution of the linearized equations proposed in [1] and with numerical results obtained with other numerical methods, see e.g. [4]. It is to be remarked that for this experiment 300×10 elements, $p^\pi = 4$, $p^u = 5$ and a timestep $\Delta t = 15$ s were used, corresponding to a Courant number $C_{snd} \approx 25$.

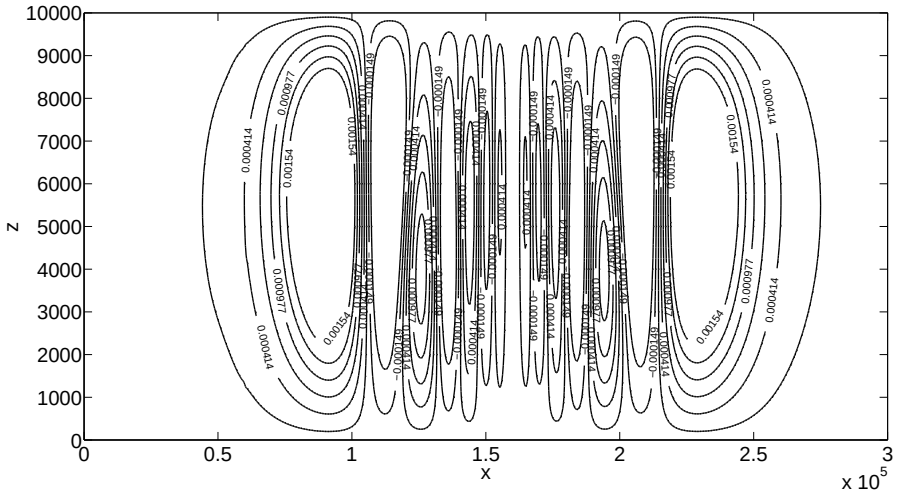

Figure 16: Contours of perturbation potential temperature in the internal gravity wave test.

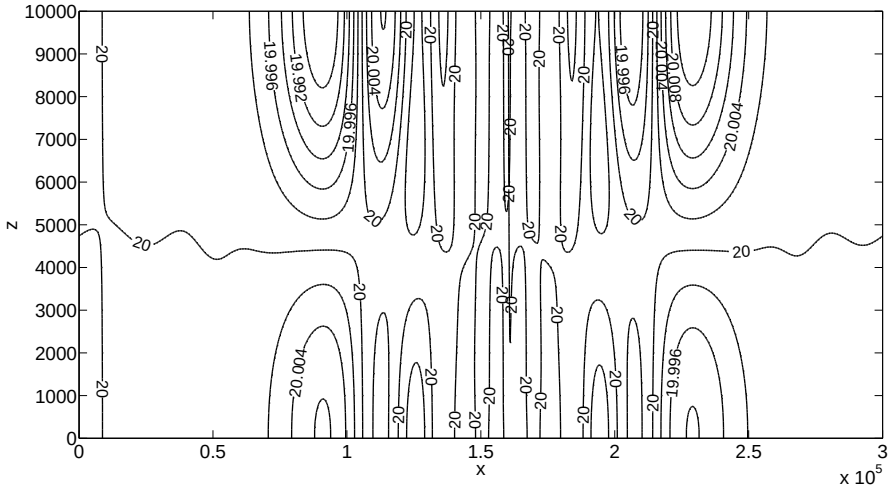

Figure 17: Contours of horizontal velocity in the internal gravity wave test.

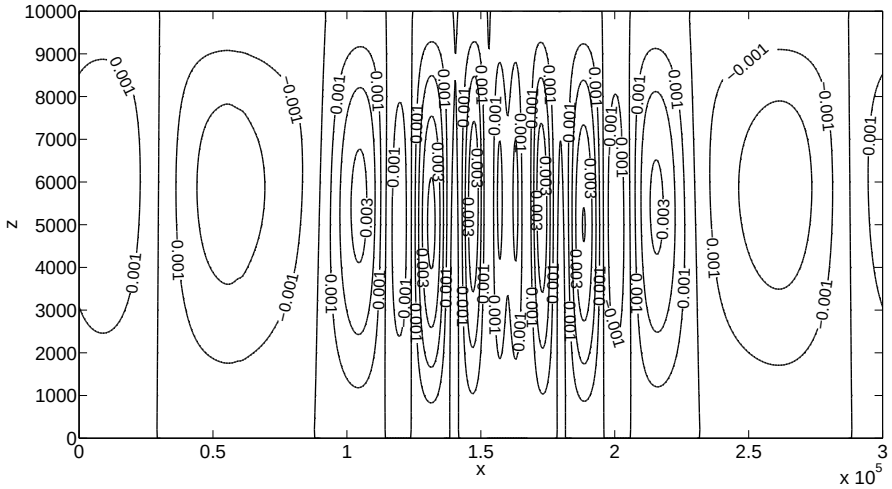

Figure 18: Contours of vertical velocity in the internal gravity wave test.

7.6 Rising thermal bubble

As nonlinear nonhydrostatic time-dependent experiment, we consider in this section the test case proposed in [23]. It consists in the evolution of a warm bubble placed in an isentropic atmosphere at rest. All data are as in [23]. Contours of potential temperature perturbation at different times are shown in figure 19. These results were obtained using 64×80 elements, $p^\pi = 4$, $p^u = 5$ and a timestep $\Delta t = 0.5$ s, corresponding to a Courant number $C_{snd} \approx 17$.

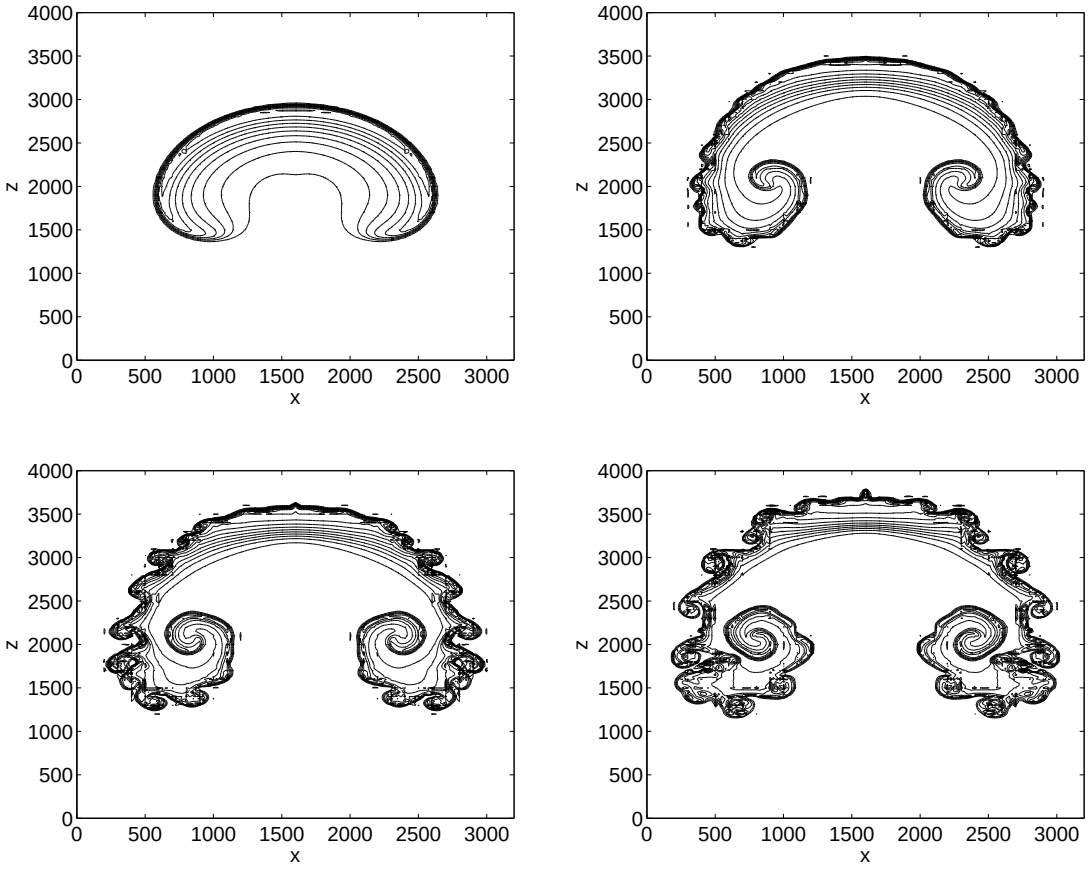

Figure 19: Contours (every 0.2 K and the zero contour is omitted) of perturbation potential temperature in the rising thermal bubble test at time 10 min, 14 min, 15 min and 16 min respectively in clockwise sense.

8 Conclusions and future perspectives

We have introduced an accurate and efficient discretization approach for typical model equations of atmospheric flows. We have extended to spherical geometry the techniques proposed in [52], combining a semi-Lagrangian approach with the TR-BDF2 semi-implicit time discretization method and with a spatial discretization based on adaptive discontinuous finite elements. The resulting method is unconditionally stable and has full second order accuracy in time, thus improving standard off-centered trapezoidal rule discretizations without any major increase in the computational cost nor loss in stability, while allowing the use of time steps up to 100 times larger than those required by stability for explicit methods applied to corresponding DG discretizations. The method also has arbitrarily high order accuracy in space and can effectively adapt the number of degrees of freedom employed in each element in order to balance accuracy and computational cost. The $p-$adaptivity approach employed does not require remeshing and is especially suitable for applications, such as numerical weather prediction, in which a large number of physical quantities is associated to a given the mesh.

Furthermore, although the proposed method can be implemented on arbitrary unstructured and nonconforming meshes, like reduced Gaussian grids employed by spectral transform models, even in applications on simple Cartesian meshes in spherical coordinates the $p-$adaptivity approach can cure effectively the pole problem by reducing the polynomial degree in the polar elements, yielding a reduction in the computational cost that is comparable to that achieved with reduced grids. Numerical simulations of classical shallow water and non-hydrostatic benchmarks have been employed to validate the method and to demonstrate its capability to achieve accurate results even at large Courant numbers, while reducing the computational cost thanks to the adaptivity approach. The proposed numerical framework can thus provide the basis of for an accurate and efficient adaptive weather prediction system.

Acknowledgements

This research work has been supported financially by the The Abdus Salam International Center for Theoretical Physics, Earth System Physics Section. We are extremely grateful to Filippo Giorgi of ICTP for his strong interest in our work and his continuous support. Financial support has also been provided by the INDAM-GNCS 2012 project *Sviluppi teorici ed applicativi dei metodi Semi-Lagrangiani* and by Politecnico di Milano. We would also like to acknowledge useful conversations on the topics of this paper with C. Erath, F. X. Giraldo, M. Restelli, N. Wood.

References

[1] M. Baldauf and S. Brdar. An analytic solution for linear gravity waves in a channel as a test for numerical models using the non-hydrostatic, compressible Euler equations. *Quarterly Journal of the Royal Meteorological Society*, 139:1977–1989, 2013.

[2] R.E. Bank, W.M. Coughran, W. Fichtner, E.H. Grosse, D.J. Rose, and R.K. Smith. Transient Simulation of Silicon Devices and Circuits. *IEEE Transactions on Electron Devices.*, 32:1992–2007, 1985.

[3] J.R. Bates, F.H.M. Semazzi, R.W. Higgins, and S.R.M. Barros. Integration of the Shallow Water Equations on the Sphere Using a Vector Semi-Lagrangian Scheme with a Multigrid Solver. *Monthly Weather Review*, 118:1615–1627, 1990.

[4] L. Bonaventura. A semi-implicit, semi-Lagrangian scheme using the height coordinate for a nonhydrostatic and fully elastic model of atmospheric flows. *Journal of Computational Physics*, 158:186–213, 2000.

[5] L. Bonaventura, R. Redler, and R. Budich. *Earth System Modelling 2: Algorithms, Code Infrastructure and Optimisation.* Springer Verlag, New York, 2012.

[6] J. Butcher and D. Chen. A new type of singly-implicit Runge-Kutta method. *Applied numerical mathematics*, 34:179–188, 2000.

[7] V. Casulli and E. Cattani. Stability, accuracy and efficiency of a semi-implicit method for three-dimensional shallow water flow. *Computational Mathematics and Applications*, 27:99–112, 1994.

[8] J. Coté. A Lagrange multiplier approach for the metric terms of semi-Lagrangian models on the sphere. *Quarterly Journal of the Royal Meteorological Society*, 114:1347–1352, 1988.

[9] J. Coté and A. Staniforth. A Two-Time-Level Semi-Lagrangian Semi-implicit Scheme for Spectral Models. *Monthly Weather Review*, 116:2003–2012, 1988.

[10] M.J.P. Cullen. A test of a semi-implicit integration technique for a fully compressible non-hydrostatic model. *Quarterly Journal of the Royal Meteorological Society*, 116:1253–1258, 1990.

[11] T. Davies, M.J.P. Cullen, A.J. Malcolm, M.H. Mawson, A. Staniforth, A.A. White, and N. Wood. A new dynamical core for the Met Office's global and regional modelling of the atmosphere. *Quarterly Journal of the Royal Meteorological Society*, 131:1759–1782, 2005.

[12] C.N. Dawson, J.J. Westerink, J.C. Feyen, and D. Pothina. Continuous, Discontinuous and coupled Discontinuous-Continuous Galerkin finite element methods for the shallow water equations. *International Journal of Numerical Methods in Fluids*, 52:63–88, 2006.

[13] F. Desharnais and A. Robert. Errors near the poles generated by a semi-Lagrangian integration scheme in a global spectral model. *Atmosphere-Ocean*, 28:162–176, 1990.

[14] M. Dumbser and V. Casulli. A staggered semi-implicit spectral discontinuous Galerkin scheme for the shallow water equations. *Applied Mathematics and Computation*, 219(15):8057 – 8077, 2013.

[15] A.E. Gill. *Atmospheric-Ocean Dynamics.* Academic Press, 1987.

[16] F.X. Giraldo. Trajectory computations for spherical geodesic grids in cartesian space. *Monthly Weather Review*, 127:1651–1662, 1999.

[17] F.X. Giraldo, J.S. Hesthaven, and T. Warburton. High-Order Discontinuous Galerkin methods for the spherical shallow water equations. *Journal of Computational Physics*, 181:499–525, 2002.

[18] F.X. Giraldo, J.F. Kelly, and E.M. Constantinescu. Implicit-explicit formulations of a three-dimensional nonhydrostatic unified model of the atmosphere (NUMA). *SIAM Journal of Scientific Computing*, 35(5):1162–1194, 2013.

[19] F.X. Giraldo and M. Restelli. High-order semi-implicit time-integrators for a triangular discontinuous Galerkin oceanic shallow water model. *International Journal of Numerical Methods in Fluids*, 63(9):1077–1102, 2010.

[20] M. Hortal and A. Simmons. Use of reduced Gaussian grids in spectral models. *Monthly Weather Review*, 119:1057–1074, 1991.

[21] M.E. Hosea and L.F. Shampine. Analysis and implementation of TR-BDF2. *Applied Numerical Mathematics*, 20:21–37, 1996.

[22] R. Jakob-Chien, J. Hack, and D. Williamson. Spectral transform solutions to the shallow water test set. *Journal of Computational Physics*, 119:164187, 1995.

[23] R. L. Carpenter Jr., K. K. Droegemeier, P. R. Woodward, and C. E. Hane. Application of the Piecewise Parabolic Method (PPM) to Meteorological Modeling. *Monthly Weather Review*, 118:586–612, 1990.

[24] C. T. Kelley. *Iterative Methods for Linear and Nonlinear Equations.* SIAM, Philadelphia, 1995.

[25] J.F. Kelly and F.X. Giraldo. Continuous and discontinuous Galerkin methods for a scalable three-dimensional nonhydrostatic atmospheric model: Limited-area mode. *Journal of Computational Physics*, 231(24):7988–8008, 2012.

[26] C. Kennedy and M. Carpenter. Additive Runge-Kutta schemes for convection-diffusion-reaction equations. *Applied Numerical Mathematics*, 44:139–181, 2003.

[27] J.D. Lambert. *Numerical methods for ordinary differential systems.* Wiley, 1991.

[28] M. Läuter, F.X. Giraldo, D. Handorf, and K. Dethloff. A discontinuous Galerkin method for the shallow water equations in spherical triangular coordinates. *Journal of Computational Physics*, 227(24):10226–10242, 2008.

[29] M. Läuter, D. Handorf, and K. Dethloff. Unsteady analytical solutions of the spherical shallow water equations. *Journal of Computational Physics*, 210:535,553, 2005.

[30] D.Y. Le Roux. Spurious inertial oscillations in shallow-water models. *Journal of Computational Physics*, 231:7959–7987, 2013.

[31] D.Y. Le Roux and G.F. Carey. Stability-dispersion analysis of the discontinuous Galerkin linearized shallow-water system. *International Journal of Numerical Methods in Fluids*, 48:325–347, 2005.

[32] R. LeVeque. *Finite difference methods for ordinary and partial differential equations: steady-state and time-dependent problems.* Society for Industrial and Applied Mathematics, 2007.

[33] A. McDonald and J.R. Bates. Semi-Lagrangian Integration of a Gridpoint Shallow Water Model on the Sphere. *Monthly Weather Review*, 117:130–137, 1989.

[34] J.L. McGregor. Economical determination of departure points for semi-Lagrangian models. *Monthly Weather Review*, 121:221–330, 1993.

[35] K. W. Morton. On the analysis of finite volume methods for evolutionary problems. *SIAM Journal of Numerical Analysis*, 35:2195–2222, 1998.

[36] K. W. Morton, A. Priestley, and E. Süli. Stability of the Lagrange-Galerkin scheme with inexact integration. *RAIRO Modellisation Matemathique et Analyse Numerique*, 22:625–653, 1988.

[37] K. W. Morton and E. Süli. Evolution-Galerkin methods and their supraconvergence. *Numerische Mathematik*, 71:331–355, 1995.

[38] R. D. Nair, S.J. Thomas, and R.D. Loft. A Discontinuous Galerkin Global Shallow Water Model. *Monthly Weather Review*, 133:876–888, 2005.

[39] R. D. Nair, S.J. Thomas, and R.D. Loft. A Discontinuous Galerkin transport scheme on the cubed sphere. *Monthly Weather Review*, 133:814–828, 2005.

[40] A. Priestley. Exact Projections and the Lagrange-Galerkin Method: A Realistic Alternative to Quadrature. *Journal of Computational Physics*, 112:316–333, 1994.

[41] M. Restelli, L. Bonaventura, and R. Sacco. A semi-Lagrangian Discontinuous Galerkin method for scalar advection by incompressible flows. *Journal of Computational Physics*, 216:195–215, 2006.

[42] M. Restelli and F.X. Giraldo. A conservative Discontinuous Galerkin semi-implicit formulation for the Navier-Stokes equations in nonhydrostatic mesoscale modeling. *SIAM Journal of Scientific Computing*, 31:2231–2257, 2009.

[43] P. Ripodas, A. Gassmann, J. Förstner, D. Majewski, M. Giorgetta, P. Korn, L. Kornblueh, H. Wan, G. Zängl, L. Bonaventura, and T. Heinze. Icosahedral Shallow Water Model (ICOSWM): results of shallow water test cases and sensitivity to model parameters. *Geoscientific Model Development*, 2:231–251, 2009.

[44] H. Ritchie. Application of the Semi-Lagrangian Method to a Spectral Model of the Shallow Water Equations. *Monthly Weather Review*, 116:1587–1598, 1988.

[45] G. Rosatti, L. Bonaventura, and D. Cesari. Semi-implicit, semi-Lagrangian environmental modelling on cartesian grids with cut cells. *Journal of Computational Physics*, 204:353–377, 2005.

[46] Y. Saad and M.H. Schultz. GMRES: A generalized minimal residual algorithm for solving nonsymmetric linear systems. *SIAM Journal on Scientific and Statistical Computing*, 7:856–869, 1986.

[47] W.C. Skamarock and J.B. Klemp. Efficiency and accuracy of the Klemp-Wilhelmson time-splitting technique. *Monthly Weather Review*, 122:2623–2630, 1994.

[48] A. Staniforth, A.A. White, and N. Wood. Treatment of vector equations in deep-atmosphere semi-Lagrangian models.I: Momentum equation. *Quarterly Journal of the Royal Meteorological Society*, 136:497–506, 2010.

[49] C. Temperton, M. Hortal, and A. Simmons. A two-time-level semi-Lagrangian global spectral model. *Quarterly Journal of the Royal Meteorological Society*, 127:111–127, 2001.

[50] J. Thuburn and Y. Li. Numerical simulations of Rossby-Haurwitz waves. *Tellus A*, 52:181189, 2000.

[51] J. Thuburn and A.A. White. A geometrical view of the shallow-atmosphere approximation, with application to the semi-lagrangian departure point calculation. *Quarterly Journal of the Royal Meteorological Society*, 139:261268, 2013.

[52] G. Tumolo, L. Bonaventura, and M. Restelli. A semi-implicit, semi-Lagrangian, p-adaptive discontinuous Galerkin method for the shallow water equations. *Journal of Computational Physics*, 232:46–67, January 2013.

[53] R.A. Walters. Numerically induced oscillations in finite-element approximations to the shallow-water equations. *International Journal of Numerical Methods in Fluids*, 3:591–604, 1983.

[54] R.A. Walters and G.F. Carey. Analysis of spurious oscillation modes for the shallow-water and Navier-Stokes equations. *Computers and Fluids*, 11:51–68, 1983.

[55] D.L. Williamson, J.B. Drake, J.J. Hack, R. Jacob, and P.N. Swarztrauber. A Standard Test Set for the Numerical Approximations to the Shallow Water Equations in Spherical Geometry. *Journal of Computational Physics*, 102:211–224, 1992.

[56] O.C. Zienkiewicz, J.P.Gago, and D.W. Kelly. The hierarchical concept in finite element analysis. *Computers and Structures*, 16:53–65, 1983.